

Instituto Tecnológico y de Estudios Superiores de Monterrey

Campus Monterrey

School of Engineering and Sciences



Optical depth sectioning with quantum interferometry

A thesis presented by

Jorge Arturo Rojas Santana

Submitted to the
School of Engineering and Sciences
in partial fulfillment of the requirements for the degree of

Doctor of Philosophy

in

Nanotechnology

Monterrey, Nuevo León, May, 2021

Instituto Tecnológico y de Estudios Superiores de Monterrey

Campus Monterrey

School of Engineering and Sciences

The committee members, hereby, certify that have read the thesis presented by Jorge Arturo Rojas Santana and that it is fully adequate in scope and quality as a partial requirement for the degree of Doctor of Science in Nanotechnology.

Dr. Dorilián López Mago
Tecnológico de Monterrey
Principal Advisor

Dr. Juan P. Torres
ICFO - Institut de Ciències Fotoniques
Co-Advisor

Dr. Julio Cesar Gutiérrez Vega
Tecnológico de Monterrey
Committee Member

Dr. Alfred Barry U'Ren Cortés
Universidad Nacional Autónoma de México
Committee Member

Dr. Raúl Hernández Aranda
Tecnológico de Monterrey
Committee Member

Dr. Rubén Morales Menéndez
Dean of Graduate Studies
School of Engineering and Sciences

Monterrey, Nuevo León, May, 2021

Declaration of Authorship

I, Jorge Arturo Rojas Santana, declare that this thesis titled, "Optical depth sectioning with quantum interferometry" and the work presented in it are my own. I confirm that:

- This work was done wholly or mainly while in candidature for a research degree at this University.
- Where any part of this thesis has previously been submitted for a degree or any other qualification at this University or any other institution, this has been clearly stated.
- Where I have consulted the published work of others, this is always clearly attributed.
- Where I have quoted from the work of others, the source is always given. With the exception of such quotations, this dissertation is entirely my own work.
- I have acknowledged all main sources of help.
- Where the thesis is based on work done by myself jointly with others, I have made clear exactly what was done by others and what I have contributed myself.

Jorge Arturo Rojas Santana
Monterrey, Nuevo León, May, 2021

©2021 by Jorge Arturo Rojas Santana
All Rights Reserved

Dedication

I want to dedicate this work to all people who have unconditionally helped me, especially my professors, friends, siblings, and parents. Unfortunately, some of them will not be able to read these lines. I send my more profound gratitude to them wherever you are. Without you, this achievement would not have been possible.

Acknowledgements

I want to express my deepest gratitude to Dr. Dorilián López-Mago for being an excellent professor. Thank you for the support to learn more about the beautiful world of science and for dedicating all this valuable time to encourage me to discover and overcome the limits of my understanding. Thanks to Dr. Juan P. Torres for sharing your time and knowledge with me. I enjoyed a lot the opportunity to be part of the Physics Optics Group and the Quantum Engineering of Light Group.

Thanks to my colleagues and friends Israel, Job, Carlos, Rafa, Uriel, Balderas, Manuel, Mateouz, Adad, and Gerard for the great times and discussions. You were the support in difficult times and a source of inspiration. Thanks to all my friends that from a distance, helped me through the most challenging times. I know that time and space only make our friendship stronger. I want to give Noe and his entire family special thanks for welcoming me into your home in Castelldefels and sharing beautiful moments with me. Thank you very much for everything.

In these difficult times, I could back home sooner than I expected and enjoy the company of my family, especially great moments with my nieces Mildred and Paolita. I have no words to thank my mom and dad for all the good advice they have given me. Thanks to you, I have managed to fulfill all my dreams. I hope to honor your great example by giving my best every day to build a better world.

Finally, my deepest gratitude to the Mexican educational system because thanks to its noble mission, I was able to study to improve myself. Thank you, CONACYT, Tecnológico de Monterrey, and all the national and international institutions that gave me their support to achieve my Ph. D. in Nanotechnology.

Optical depth sectioning with quantum interferometry

by

Jorge Arturo Rojas Santana

Abstract

The optical depth sectioning is a methodology to study the internal structure of semitransparent materials. Optical coherence tomography (OCT) is the standard technique for this purpose. Recent advances on OCT based on quantum principles transform the technique's physics, giving potential capabilities to develop more robust systems.

OCT has demonstrated exceptional performance; however, the demand for increasingly precise systems encourages new developments. The challenge is to eliminate the effects that distort images, such as chromatic dispersion or low resolution. A potential solution is found in new OCT systems considering non-classical light sources, nonlinear interferometers, and singular photon detection systems. The development of these systems poses challenges in multiple aspects such as theoretical, experimental, and technical. This thesis gives three main contributions. The first is developing a detection methodology to use an oscilloscope as a cost-effective solution for counting and timing photons.

The second contribution is a theoretical framework to realize optical coherence tomography using nonlinear interferometers such as OCT in an SU (1,1) interferometer, OCT based on induced coherence, and quantum-OCT working in the Fourier domain. We deduced general expressions for the output spectrum and focused our analysis on the particular case of a bi-layer sample. Our formulation allows us to perform a peer comparison, showing the main similarities and differences between the techniques. These results add valuable information to the growing body of literature concerning applications of nonlinear interferometers.

Finally, we study an experiment of the induced coherence tomography to understand the role of the pump pulses in defining the spatial resolution of the system. We found the possibility of achieving high spatial resolutions and high emission rates by combining ultrashort pumping with millimeter-length crystals maintaining its advantageous features, i.e., probing the sample with high-resolution ideal wavelength and using the optimum wavelength for detection.

List of Figures

2.1	The three main components of an optical coherence tomography system. . . .	5
2.2	(a) Time domain and (b) Fourier domain-OCT schemes. Here the input light of broad bandwidth is split into a reference and testing beams. The interference between the beams reveals the depth profile of the sample. Time domain-OCT uses a movable mirror to detect the intensity $I(\tau)_{\text{TDOCT}}$ doing a scan in the propagation axis z where the time difference of the optical paths is τ . Fourier domain-OCT has no moving parts; the sample is placed at a distance s to capture the spectrum $S(k)_{\text{FDOCT}}$	6
2.3	(a) Spectral density of a Gaussian light source $\Phi(k = 2\pi/\lambda)_{\text{gauss}}$, centered at k_0 and bandwidth Δk . (b) Multi-layer material with different refractive indices n 's immersed in a medium with refractive index n_0 . τ_1 is the time for a round-trip of the light in the layer of thickness d_1	7
2.4	Interferogram $I(\tau)_{\text{TDOCT}}$ of a glass plate with thickness $100\mu\text{m}$ and refractive index of 1.5. For a light source of Gaussian spectrum centered at $\lambda_0 = 810\text{nm}$ and coherence length of: (a) $22.7\mu\text{m}$ and (b) $227.5\mu\text{m}$	8
2.5	Spectrogram of a glass plate of thickness $100\mu\text{m}$ and refractive index 1.5. (a,c) Normalized spectral density $S(k = \Omega/c)_{\text{FDOCT}}$. (b, d) Fourier transform $ \hat{S}(z = 2\pi/k)_{\text{FDOCT}} $. For a light source of Gaussian spectrum centered at $\lambda_0 = 810\text{nm}$ and coherence length of: (up) $22.7\mu\text{m}$ and (down) $227.5\mu\text{m}$. . .	10
2.6	Components of a quantum inspired OCT systems.	11
2.7	Bi-photon source. A pump photon of frequency ω_p propagating inside a nonlinear crystal is spontaneously down-converted in two photons of frequency ω_s and ω_i . The photon pair generation is (a) collinear with degenerate photons ($\omega_s = \omega_i$), (b) collinear with nondegenerate photons ($\omega_s \neq \omega_i$), (c) non-collinear with degenerate photons, and (d) noncollinear with nondegenerate photons.	12
2.8	Nonlinear Mach-Zehnder interferometer with two bi-photon sources to study the induce coherence effect [28]. The interference of photons s_1 and s_2 depends on the transmissivity of the filter NDF. The visibility of the interference varies periodically, moving the beamsplitter. Curve A: filter with a transmissivity of 0.91. Curve B: filter with a transmissivity of 0.	13
2.9	Hong-Ou-Mandel interferometer to study the two-photon interference [72]. Inducing a time delay moving the beamsplitter (BS), the detection of photon coincidences measures the photon interference giving a minimum (HOM deep) when the optical paths are equal.	14

3.1	Experimental setup of an entangled twin-photon source. Here the photons of wavelength centered at 405 nm are transformed in two of 810 nm. The components are a polarizing beamsplitter (PBS), mirrors (M1 and M2), filter at 405 nm (Fi), beamsplitter (BS), a flip mirror (FM), Type I BBO crystal, linear polarizer, filters at 780 nm and (810 ± 5) nm (F), collectors (A and B), multimode fibers (OF) and single-photon counting modules (SPCMs) and an oscilloscope for photo timing.	17
3.2	Oscilloscope wavefront of a transistor-transistor logic (TTL) output pulse with time scale (10 ns/div) and frequency (156 Hz). The pulse has a width of 10 ± 2 ns and the side oscillations are attributed to partial reflections from the electrical connections.	18
3.3	(a) Modeling of the pulse trains of single photons. (b) Time window (τ) for photon counting the photon pairs. (c) Pulse detection with resolution of 1 ns (dot) and its interpolation to achieve a resolution of 5 ps (line).	19
3.4	Simulation of the hitogram of coincidences with bin size of 1 ns for (a) time-correlated photons and (b) time-uncorrelated photons.	20
3.5	Measurement of the histogram of coincidences with bin size of (a) time-correlated photons, and (b) time-uncorrelated photons.	21
3.6	Delay effect in the histogram of coincidences of time-correlated photons with (a) Bin size of 1 ns from experimental data and (b) Bin size of 5 ps from experimental data fitting. The pulse duration defines the broadest coincidence time windows. The pulse resolution is 1 ns and 5 ps respectively.	22
4.1	Fourier domain OCT with a SU(1,1) interferometer scheme. Here, a laser pumps the nonlinear crystal generating a pair of entangled photons: signal (s_1) and idler (i_1). The dichroic mirror separates the pump, signal, and idler photons. The photons are reflected, and after the second pass of the pump through the nonlinear crystal, the new signal photons s_2 are correlated with the first ones detected by the spectrometer Sp.	26
4.2	Fourier domain induced coherence tomography scheme in a type Mach Zehnder interferometer.	28
4.3	Fourier domain quantum-optical coherence tomography scheme in a Hong–Ou–Mandel interferometer. Here, a monochromatic laser of frequency ω_p pumps a nonlinear crystal (NLC) generating frequency entangled photons s_1 and s_2 . After the beamsplitter, the spectrogram $S(k)_{\text{FDQOCT}}$ is acquired by a bi-photon spectrometer.	30
4.4	The left column shows the output spectrum $S(k = \Omega/c)$ for all the methods under study. The right column shows the Fourier transform of the spectrum. We only display the positive z-axis due to the symmetry of $ \hat{S}(z = 2\pi/k) ^2$	32
4.5	The amplitude of the interface contrasts for the reflectance of the reference mirror R_R in the interferometer. Self-interference terms: (+) Standard OCT and (line) QOCT. Cross-correlated interference terms for the first layer R_0 : (dot) Standard OCT, (dot-line) QOCT, (line) SU(1,1) and ICT.	33

5.1	Induced coherence between signal photons generated in separate parametric down converters. The idler traverses a lossy sample before being injected into NLC2. The detector measures the interference between signal photons s_1 and s_2 as a function of the path delay Δz . NLC: nonlinear crystal; s, i : signal and idler modes; b, a input and output quantum operators.	36
5.2	Triangular (red dotted line) and Gaussian (solid blue line) functions describing the degree of first-order coherence $g_{s_1, s_2}^{(1)}$ [Eq. (5.39)]. We consider nonlinear crystals with lengths $L = 5$ mm (first row) and $L = 10$ mm (second row) and a pumping pulsed laser of (a) $T_0 = 100$ ps, (b) $T_0 = 2$ ps, and (c) $T_0 = 100$ fs.	43
5.3	(a) Coherence length in terms of the pulse width T_0 . (b) The bandwidth of the signal-photon spectrum. We consider nonlinear crystals with lengths $L = 5$ mm (black dotted lines) and $L = 10$ mm (blue solid lines).	44
5.4	Signal N in one output port of the beamsplitter as a function of Δz for a bi-layer sample (first row). We assume a $20 \mu\text{m}$ glass slab with a refractive index $n = 1.5$ embedded between air and water. We consider three different combinations for the length L of the nonlinear crystals and pump pulses duration T_0 . (a) $L = 0.5$ mm, $T_0 = 100$ ps, (b) $L = 10$ mm, $T_0 = 100$ ps, and (c) $L = 10$ mm, $T_0 = 100$ fs. For illustrative purposes, we consider fringes oscillating with a wavelength larger than the actual signal-photon wavelength of 810 nm. The second row shows the normalized spectrum of the signal photon of bandwidths (d) 14.8 nm, (e) 0.8 nm and (f) 20 nm.	47

List of Tables

3.1	Coincidence measurements in function of the pump power. P is the pump power, F frequency and JCR joint current rate.	22
-----	--	----

Contents

Abstract	vii
List of Figures	x
List of Tables	xi
1 Introduction	1
1.1 Motivation	1
1.2 Context	1
1.3 Problem Statements	2
1.4 Research question and solution overview	3
1.5 Thesis overview	3
2 Background	5
2.1 Introduction to optical coherence tomography	5
2.1.1 Time-domain optical coherence tomography	6
2.1.2 Fourier-domain optical coherence tomography	9
2.2 Elements of OCT based on quantum principles	11
2.2.1 Bi-photon source	11
2.2.2 Nonlinear interferometers	12
2.2.3 Induced coherence effect	13
2.2.4 Hong-Ou-Mandel effect	14
2.3 Summary	14
3 Photon counting and timing using an oscilloscope	16
3.1 Introduction	16
3.2 Methodology	17
3.2.1 Twin-photon source	17
3.2.2 Single photon detection	18
3.2.3 Simulation of photon coincidences	19
3.3 Experimental results	20
3.3.1 Photon coincidences	20
3.3.2 Optical path photon delay	21
3.3.3 Joint current rate	22
3.4 Conclusions	23

4	OCT based on nonlinear interferometers	24
4.1	Introduction	24
4.2	OCT in a SU(1,1) interferometer	25
4.2.1	Spectrogram FD-OCT in a SU(1,1) interferometer	27
4.3	Induced Coherence Tomography	28
4.3.1	Spectrogram FD-ICT	29
4.4	Quantum OCT	29
4.4.1	Spectrogram FD-QOCT	30
4.5	Results	31
4.5.1	Fourier domain spectrograms	31
4.5.2	Interface contrast	33
4.6	Conclusions	34
5	Tailoring the axial resolution in induced coherence tomography	35
5.1	Introduction	35
5.2	Formalism	36
5.2.1	Interferogram	39
5.2.2	The normalized first-order correlation function	39
5.3	Results	42
5.3.1	Axial resolution	42
5.3.2	Coherent length and bandwidth	43
5.3.3	Time domain induce coherence tomography of a bi-layer sample	44
5.4	Conclusions	47
6	Conclusions and future work	49
6.1	Conclusions	49
6.2	Future work	50
	Bibliography	61

Chapter 1

Introduction

1.1 Motivation

Advance systems for optical depth sectioning based on quantum principles demonstrate high axial resolutions and new detection schemes for scientific and potential clinical applications. The long acquisitions times are a limitation for its applications under scenarios of fast detection. The motivation of my work is to reduce the image acquisition times without the detriment of the high axial resolution. In my view, develop new single-photon detection methods and optimize the optical system are critical aspects for designing systems with optimal efficiency and acquisition times.

1.2 Context

The optical depth sectioning is a methodology to study the internal structure of materials. Imaging techniques such as optical sectioning microscopy [1] and optical coherence tomography [2] allow the acquisition of 3D images with a high lateral and axial resolution.

Optical Coherence Tomography (OCT) is a widely used technique for imaging the internal structure of semitransparent materials [3]. This non-invasive and non-destructive technique has a penetration power of millimeters and axial resolution of micrometers, ideal characteristics for medical diagnosis [2, 4]. Year after year its applications grow in fields such as ophthalmology [5, 6, 7], endoscopy [8], dermatology [9], cardiology [10], neurosciences [11], having a great scientific, clinical and economic impact [12, 13, 14].

The need for high precision images demands the development of new systems with better performance. In 1991 Huang *et al.* presented the first OCT system (Time Domain-OCT), starting the successful race of this technique [15]. Years later, in 1995, Fercher *et al.* developed a new version called OCT in the Fourier domain (FD-OCT) with better performance for the image acquisition speed [16]. These techniques established OCT as the standard technology in optical depth sectioning for axial super-resolution imaging [17].

The axial resolution is the capacity to distinguish between the inner structures in the sample. The high resolution allows the acquisition of high-quality images, making it easier to analyze the information. However, scattering, chromatic dispersion, and light absorption limit the resolution and penetration power of light to capture the images. Therefore, avoid them is

a fundamental challenge for design more robust OCT systems.

A typical OCT system has three components: a low coherence light source, a Michelson interferometer, and the detection system. The light source defines the axial resolution system. Developing better light sources [18, 19], detection methods [20, 21, 22] and image processing [23, 24, 25] are very active areas that can increased OCT capabilities.

Implementing non-classical light sources transforms the physics of OCT to take advantage of the quantum properties of light. The photons' quantum entanglement gives rise to the Hong-Ou-Mandel (HOM) effect [26, 27] and the induced coherence [28]. With the HOM effect is possible to increase the image's resolution by a factor of two compared to a traditional OCT system and capture images free of chromatic dispersion [29, 30, 31]. The induced coherence has shown the possibility to capture images using ideal photons to analyze the sample, but detecting photons in the optimal detection band [32, 33]. This technique is known as imaging with undetected photons. It makes it possible to minimize the scattering of light, increase penetration power, and obtain better image quality.

Advances in OCT systems based on quantum principles are promising for real-life applications [34]. However, improving the detection speed, the system's portability, and reducing its components' cost remains a challenge. We raise the following points to overcome these limitations.

1.3 Problem Statements

The approaches to contribute in the field are:

- Photon counting and timing are generic tasks in quantum optics experiments such as quantum-based OCTs. The high cost of commercial photon coincidence counters can be a limiting factor in developing or establishing quantum interferometry laboratories. There are low-cost solutions, but their construction can be tedious, especially if the interest is not in electronics. For this reason, it is desirable to have affordable and easy-to-operate detection systems.
- Users and companies need to know the quantum-based OCT technique's performance. The most promising techniques are OCT in a SU (1,1) interferometer, OCT based on induced coherence (also known as Induce Coherence Tomography, ICT), and quantum OCT (QOCT). The differences between configurations and operating principles provide images with different information. The understanding of the acquired images brings the elements for the image interpretation. This analysis could project these techniques between the users.
- Induced coherence tomography (ICT) is a technique for imaging with undetected photons where the crystal length in its configuration defines the axial image resolution. The use of tiny crystals provides higher axial resolution but increases image acquisition times. It is interesting to study the possibility of designing a high-resolution system using long crystals without detriment to the image acquisition speed.

1.4 Research question and solution overview

- Is it possible to have more affordable and easy-to-operate photon counting and timing systems?

Yes, a system for photon counting and timing has a photon counter and single photon detectors. Implement an oscilloscope as a time-correlated photon coincidence counter provides the advantage of saving the data for post-processing of the histogram of coincidences used in quantum interference experiments.

- How is the image in the quantum-based OCT techniques?

The quantum-based OCT techniques can work in the Time-domain (TD) and Fourier-domain (FD). The image information is presented in an interferogram for TD and a spectrogram for FD. We simulate the image acquisition of a bi-layer sample for the FD-OCT in a SU (1,1) interferometer, Induced coherence tomography, and quantum OCT under similar conditions to analyze the differences between images.

- Is it possible to enhance the axial image resolution and acquisition speed in a system of induced coherence tomography?

Yes, we can use femtosecond laser pulses combined with long-length crystals to increase the system's axial resolution while having a high emission rate of photon pairs and consequently reducing acquisition times.

1.5 Thesis overview

This thesis consists of 6 chapters. The motivation of this work is in chapter 1 and chapter 2 introduce the principles of classical OCT in the Time and Fourier domain and the elements that give rise to their quantum versions. Also, it is presented a brief study of the entangled photon pairs' sources and the non-linear interferometers. Both components are essential for introducing quantum interferometry effects of Hong-Ou-Mandel and induced coherence. These effects are the heart of the quantum-based OCT techniques for optical depth sectioning.

Chapter 3 presents the experimental study of time-correlated photon pairs generated by the process of spontaneous parametric down-conversion (SPDC). The simulation of entangled photon trains allowed the formulation of the methodology for measuring photon pair coincidences using an oscilloscope. The method was validated by measuring the histogram of coincidences for a classical and a quantum light source. The principal results are published in the paper "Technical aspects for counting and timing photons with a digital oscilloscope," in *Appl. Opt.* 58, 4047-4051 (2019).

Chapter 4 contains the study of OCT based on nonlinear interferometers. We present the configurations and mathematical expressions for SU (1,1), ICT, and QOCT techniques in the Fourier domain. The simulation of the spectrograms of a bi-layer sample gives the elements to understand and interpret the images obtained for each method.

Chapter 5 focuses on studying the time domain induced coherence tomography (TD-ICT), modeling the system with a pulsed pump to generate entangled photon pairs. Following the Bogoliubov formalism, we study the quantum interference and the first-order correlation.

The results showed the conditions to tailor the axial resolutions and photon fluxes for a better quality image. The main results were published in the paper "Frequency-correlation requirements on the bi-photon wave function in an induced-coherence experiment between separate sources," in Phys. Rev. A 102, 053711.

The final chapter presents the conclusions and future perspectives for developing the optical depth sectioning quantum technologies.

Chapter 2

Background

This chapter presents the formalism of the OCT in the Time domain and Fourier Domain regimes. We simulate the tomographic images of a bi-layer sample in both regimes. Afterward, we explore the elements for quantum-based OCT systems, such as entangled photon sources and nonlinear interferometers. Under this context, we review the pioneer works on photon interference of Mandel *et al.* of the induced coherent and the Hong-Ou-Mandel effects, which are the heart of the quantum optical depth sectioning techniques. At the end of this chapter, we summarize the main concepts to understand the similarities between the classical and quantum versions of OCT.

2.1 Introduction to optical coherence tomography

Optical coherence tomography (OCT) is a well-established imaging technique that produces tomographic images of materials by measuring back-reflected light [2]. This technique has practical advantages, such as noninvasive and fast testing with unique applications for *in vivo* medical diagnostics [35, 36, 37, 38].

An OCT system consists of a light source, interferometer, and detection system, see Fig. 2.1. OCT uses a low-coherence light source in an interferometric setup where the input light splits into a reference and measuring beam. The reference beam passes through a delay and then is merged with the measuring beam reflected from the sample, as shown in Fig 2.2. The interference pattern gives information about the sample's internal structure, i.e., it reveals its axial profile. According to the measuring principle, OCT is classified into time-domain OCT (TD-OCT) or Fourier-domain OCT (FD-OCT) [15, 39].



Figure 2.1: The three main components of an optical coherence tomography system.

2.1.1 Time-domain optical coherence tomography

Figure 2.2(a) shows the TD-OCT optical array scheme. In this regime one beam after the beamsplitter (BS) travels to the movable mirror and the other to the sample under study. The reference ψ_R and sample ψ_T beams are written as

$$\begin{aligned}\psi_R(k_0 + k) &= r_{BS}t_{BS}r_R\Phi(k_0 + k)\exp(2i(k_0 + k)z_1) \\ \psi_T(k_0 + k) &= r_{BS}t_{BS}r_i(k_0 + k)\Phi(k_0 + k)\exp(2i(k_0 + k)z_2),\end{aligned}\quad (2.1)$$

where r_{BS} and t_{BS} are the reflection and transmission coefficients of the BS (for a 50:50, $|r_{BS}t_{BS}|^2 = 1/4$). $\Phi(k_0 + k)$ is the light source spectrum with $k_0 = \omega_0/c$, $k = \Omega/c$, where Ω is the frequency deviation from the central frequency ω_0 and c the speed of light in vacuum. z_1 and z_2 are the distances from the BS to the mirror and to the sample. r_R is the reflection coefficient of the reference mirror and $r_i(k)$ is the transfer function of the sample.

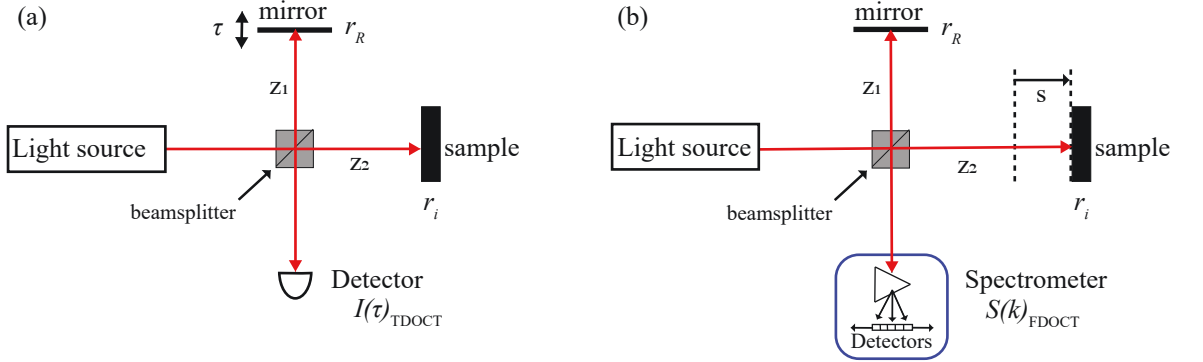


Figure 2.2: (a) Time domain and (b) Fourier domain-OCT schemes. Here the input light of broad bandwidth is split into a reference and testing beams. The interference between the beams reveals the depth profile of the sample. Time domain-OCT uses a movable mirror to detect the intensity $I(\tau)_{\text{TDOCT}}$ doing a scan in the propagation axis z where the time difference of the optical paths is τ . Fourier domain-OCT has no moving parts; the sample is placed at a distance s to capture the spectrum $S(k)_{\text{FDOCT}}$.

The reflected beams are recombined by the same BS generating their superposition expressed by

$$\Psi(k_0 + k) = \psi_R(k_0 + k) + \psi_T(k_0 + k). \quad (2.2)$$

Therefore, the spectral density is

$$S(k) = |\Psi(k_0 + k)|^2 \quad (2.3)$$

The detector measures the light intensity as a function of the time difference of the optical paths τ induced by the z -scan during the measuring process. The intensity is given by

$$I(\tau) = \int S(k)dk. \quad (2.4)$$

The eq. (2.4) describes the interferogram and depends on the light spectrum $\Phi(k)$ and sample transfer function $r_i(k)$.

OCT systems works in the ultraviolet [40], visible [41] and infrared spectrum [42]. The coherence length of the light source defines the axial resolution of the OCT system. Figure 2.3(a) shows the spectrum of a Gaussian light source, written as

$$\Phi(k)_{\text{gauss}} = \frac{1}{\sqrt{\pi^{1/2} \Delta k}} \exp\left(-\frac{k^2}{2(\Delta k)^2}\right), \quad (2.5)$$

where the bandwidth Δk is related to the spectral bandwidth $\Delta\lambda$ and the central wavelength $\lambda_0 = 2\pi/k_0$ via $\Delta k = \pi\Delta\lambda(\lambda_0^2\sqrt{\ln 2})^{-1}$. The coherence length of the light source is

$$l_c = \frac{2\sqrt{\ln 2}}{\pi} \frac{\lambda_0^2}{\Delta\lambda}. \quad (2.6)$$

The coherence length defines the longitudinal resolution $l_r = l_c/2$ which is the minimum longitudinal separation detectable in two successive distinct locations in the sample with different optical characteristics [43]. Therefore, a narrow spectral bandwidth implies large values of coherent length and worse longitudinal resolution.

Considering samples with multiple layers distinguished by their refractive index and thickness, the transfer function can be written as [2]

$$r_i(k) = r_0 + \sum_{j=1}^N r_j e^{-2in_j(k)d_j} = r_0 + r_1 e^{-2in_1(k)d_1} + r_2 e^{-2in_2(k)d_2} + \dots, \quad (2.7)$$

here r_j is the effective refraction coefficient between layers given by the Fresnel coefficients [44]. The factor 2 represents the distance traveled in a round-trip of light between layers of thickness d_j and $n_j(k) = k_0 n_{0,j} + k n_{g,j}$ where $n_{0,j}$ is the refractive index and $n_{g,j}$ the group refractive index, see Fig. 2.3(b).

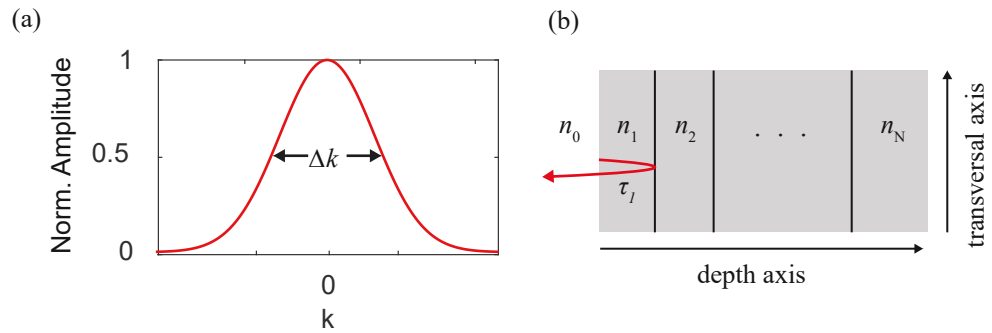


Figure 2.3: (a) Spectral density of a Gaussian light source $\Phi(k = 2\pi/\lambda)_{\text{gauss}}$, centered at k_0 and bandwidth Δk . (b) Multi-layer material with different refractive indices n 's immersed in a medium with refractive index n_0 . τ_1 is the time for a round-trip of the light in the layer of thickness d_1 .

For a bi-layer sample $N = 1$ in eq. (2.7), the transfer function is $r_i(k) = r_0 + r_1 \exp[-2i(k_0 n_{0,1} + k n_{g,1})d]$ and substituting in eq. (2.3), the spectral density for a bi-layer

sample is

$$S(k)_{\text{TDOCT}} = \frac{R_R + R_0 + R_1}{4} |\Phi(k)|^2 \left\{ 1 + \frac{2\sqrt{R_0 R_1}}{R_R + R_0 + R_1} \cos[\varphi_1 + 2n_{g,1} d k] \right. \\ \left. + \frac{2\sqrt{R_0}}{R_R + R_0 + R_1} \cos[\varphi_2 + 2c\tau k] + \frac{2\sqrt{R_1}}{R_R + R_0 + R_1} \cos[\varphi_3 + (2c\tau + 2n_{g,1} d) k] \right\} \quad (2.8)$$

with $R_{R,0,1} = |r_{R,0,1}|^2$, $\varphi_1 = 2n_{0,1} d k_0$, $\varphi_2 = 2c\tau k_0$, and $\varphi_3 = (2c\tau + 2n_{0,1} d) k_0$.

Considering a Gaussian spectrum in eq. (2.8) and substituting into eq. (2.4), the interferogram for a bi-layer sample is given by

$$I(\tau)_{\text{TDOCT}} = \frac{R_R + R_0 + R_1}{4} \left\{ 1 + \frac{\sqrt{R_0 R_1}}{R_R + R_0 + R_1} \cos[2n_{0,1} d k_0] \exp[-(n_{g,1} d \Delta k)^2] \right. \\ \left. + \frac{\sqrt{R_0}}{R_R + R_0 + R_1} \cos[2c\tau k_0] \exp[-(c\tau \Delta k)^2] \right. \\ \left. + \frac{\sqrt{R_1}}{R_R + R_0 + R_1} \cos[2(c\tau - n_{0,1} d) k_0] \exp[-(c\tau \Delta k - n_{g,1} d \Delta k)^2] \right\}. \quad (2.9)$$

Notice that the first two terms in eq. (2.9) are constant. The third and fourth terms oscillate with the central frequency $\omega_0 = ck_0$ whose envelope corresponds to a Gaussian centered at the position 0 and $n_{g,1} d$ which is the sample's optical thickness. We proceed to work with eq. (2.9).

TD-OCT interferogram

As an example of application, we simulate the interferogram of a glass plate of thickness $d = 100\mu\text{m}$ and refractive index $n_{0,1} = n_{g,1} = 1.5$ submerged in air $n_{0,0} = n_{g,0} = 1$ with $r_R = 1$. Figure 2.4 shows the interferogram using a Gaussian spectrum with central wavelength $\lambda_0 = 810\text{ nm}$, bandwidth of $\Delta\lambda = 10\text{ nm}$ and $\Delta\lambda = 1\text{ nm}$.

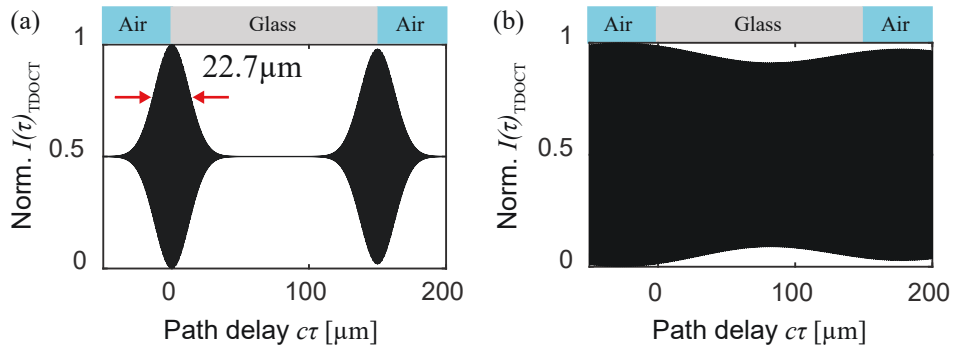


Figure 2.4: Interferogram $I(\tau)_{\text{TDOCT}}$ of a glass plate with thickness $100\mu\text{m}$ and refractive index of 1.5. For a light source of Gaussian spectrum centered at $\lambda_0 = 810\text{ nm}$ and coherence length of: (a) $22.7\mu\text{m}$ and (b) $227.5\mu\text{m}$.

Figure 2.4 shows how the bandwidth determines the coherence length and, therefore, the resolution of the system. In Fig. 2.4(a) is possible to distinguish the interface between

the air-glass-air because the coherence length of $l_c = 22.7 \mu\text{m}$ is smaller than the optical thickness of $150\mu\text{m}$. In contrast, in Fig. 2.4(b) the coherence length is $l_c = 227.4\mu\text{m}$ and the it is impossible to distinguish between interfaces. The intensity measurement $I(\tau)$ needs a scan, moving the reference mirror making a slow image acquisition. The method for a faster image acquisition arrives with the development of the Fourier domain OCT.

2.1.2 Fourier-domain optical coherence tomography

Fourier domain-OCT (FD-OCT) is the evolution of the Time domain-OCT. The main difference is that FD-OCT uses a stationary reference mirror instead of a movable mirror, as shown in Fig. 2.2(b). This change implies using a spectrometer to measure the sample's modulated spectrum $S(k)_{\text{FDOCT}}$ without the reference mirror scanning. The Fourier transform of the output spectrum $\mathcal{F}\{S(k)_{\text{FDOCT}}\}$ reveals the depth information of the sample [39].

Following the previous example where is considered a Gaussian spectrum eq. (2.5) and a bi-layer sample eq. (5.9), the spectral density in eq. (2.3) is written as

$$S(k)_{\text{FDOCT}} = \frac{R_R + R_0 + R_1}{4} |\Phi(k)_{\text{gauss}}|^2 \left\{ 1 + \frac{2\sqrt{R_0 R_1}}{R_R + R_0 + R_1} \cos[\varphi_1 + 2n_{g,1}d k] \right. \\ \left. + \frac{2\sqrt{R_0}}{R_R + R_0 + R_1} \cos[\varphi_2 + 2sk] + \frac{2\sqrt{R_1}}{R_R + R_0 + R_1} \cos[\varphi_3 + (2s + 2n_{g,1}d) k] \right\} \quad (2.10)$$

where $\Phi(k)_{\text{gauss}}$ is expressed in eq. (2.5), $s = z_2 - z_1$ is the optical path length difference, $\varphi_1 = 2n_{0,1}dk_0$, $\varphi_2 = 2sk_0$, and $\varphi_3 = (2s + 2n_{0,1}d)k_0$ are phase terms. Note that the first two contributions in eq. (2.10) are independent of s , these are referred as the self-interference terms, while the s -dependent contributions are the cross-interference terms.

The optical path difference (s) should fulfill the condition [45]

$$\frac{\lambda_0^2}{\Delta\lambda} \ll |s| \ll \frac{\lambda_0^2}{\delta\lambda}, \quad (2.11)$$

that relates the light source and the detection system, in this case, the resolution of the spectrometer $\delta\lambda$.

The Fourier transform $\hat{S}(z) = \{S(k)\}$ gives the spectrogram

$$\hat{S}(z)_{\text{FDOCT}} = \frac{R_R + R_0 + R_1}{4} \left\{ \hat{\Phi}(z) + \frac{\sqrt{R_0 R_1}}{R_R + R_0 + R_1} \exp(-i\varphi_1) \hat{\Phi}(z + 2n_{g,1}d) \right. \\ \left. + \frac{\sqrt{R_0}}{R_R + R_0 + R_1} \exp(-i\varphi_2) \hat{\Phi}(z + 2s) \right. \\ \left. + \frac{\sqrt{R_1}}{R_R + R_0 + R_1} \exp(-i\varphi_3) \hat{\Phi}(z + (2s + 2n_{g,1}d)) \right\} + c.c., \quad (2.12)$$

with $z = 2\pi/k$ and $\hat{\Phi}(z) = \mathcal{F}\{|\Phi(k)_{\text{gauss}}|^2\}$. The eq. (2.12) features seven characteristic peaks, a central peak at $z = 0$, three located at $z > 0$, and three symmetrically located at $z < 0$ defined as the conjugated components denoted by c.c. The last two terms are the cross-interference terms displaced $2n_{g,1}d$ directly yields information about the sample's optical thickness. Besides, the cross-interference depends on the delay induced by s and can be

positive or negative. It is essential to have an optical path difference $s \neq 0$ (contrary to TD-OCT where s is close to zero) to isolate the cross-interference terms with the self-interference terms. Let us now analyze the spectrogram of FD-OCT.

FD-OCT spectrogram

Following the example of TD-OCT in Fig. 2.4, the sample's modulated spectrum $S(k)_{\text{FDOCT}}$ for a glass plate positioned at $s = 300\mu\text{m}$ is presented in Fig. 2.5(a, c) and their Fourier transform to reveal the depth information can be show in Fig. 2.5(b, d). Here we consider a spectrometer's resolution of $\delta\lambda = 0.033\text{nm}$ that satisfy the condition in eq. (2.11) with values $0.065\text{mm} \ll 0.3\text{mm} \ll 19.88\text{mm}$.

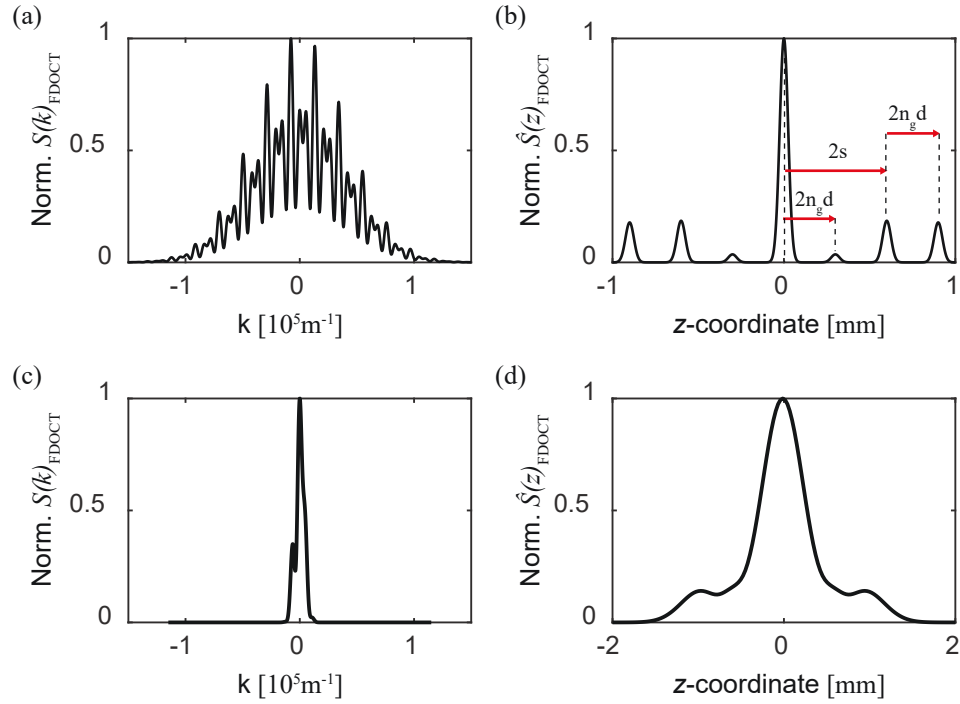


Figure 2.5: Spectrogram of a glass plate of thickness $100\mu\text{m}$ and refractive index 1.5. (a,c) Normalized spectral density $S(k = \Omega/c)_{\text{FDOCT}}$. (b, d) Fourier transform $|\hat{S}(z = 2\pi/k)_{\text{FDOCT}}|$. For a light source of Gaussian spectrum centered at $\lambda_0 = 810\text{nm}$ and coherence length of: (up) $22.7\mu\text{m}$ and (down) $227.5\mu\text{m}$.

From Fig. 2.5(b), we notice that the distance between the cross-correlated peaks is two times the sample's optical thickness ($2n_{g,1}d = 0.3\text{mm}$). Observe that the amplitude of the self-correlated peak is lower than the cross-correlated peaks. If the optical path difference $s < 2n_{g,1}d$ the self-correlation peaks may overlap with the cross-correlation peaks, making the interpretation of the spectrogram difficult or confusing. Figure 2.5(d) expose the case when the coherence length is bigger than the optical thickness given a misunderstanding figure.

The simulations of Fig. 2.4 and Fig. 2.5 show the interferograms and spectrograms obtained with TD-OCT and FD-OCT. Both results give information on the sample's internal

structure, i. e., the location of the interfaces between media with different refractive indices for deducing the optical thickness. Moreover, they demonstrate how the bandwidth of the source determines the axial resolution of the image.

The previous sections present how OCT works, and the following section presents how the OCT technique changes by implementing a light source of entangled photon pairs.

2.2 Elements of OCT based on quantum principles

Quantum inspired OCT systems are revolutionary techniques for axial super-resolution tomographic imaging. These techniques take advantage of the quantum correlations between down-converted photons to improve the standard OCT imaging system's performance. The enhancement in resolution, immunity to chromatic dispersion [29, 30, 31], and new photodetection schemes allow to obtain higher quality images [32, 33]. However, image acquisition requires more complex systems where the long acquisition times are a point of improvement.

The components for a quantum system include a nonclassical light source, a nonlinear interferometer, and a single photon detection system, see Fig. 2.6. The idea is analogous to classical OCT but in this case the interference of single photons is the mechanism for the image acquisition. Here, a nonclassical light source generates entangled photons, commonly using a nonlinear crystal to generate photon pairs by spontaneous parametric down-conversion (SPDC) [46]. The photons enters in an interferometric array which can be classified as a nonlinear interferometer for using a nonlinear crystal where SPDC take place [47]. The single photon detection system measure the photon interference [48]. Let us now to proceed with

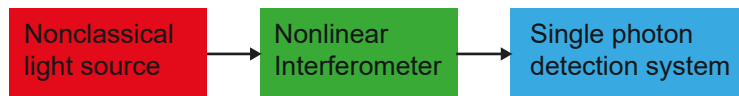


Figure 2.6: Components of a quantum inspired OCT systems.

the description of a nonclassical light source.

2.2.1 Bi-photon source

The most used method to generate entangled photon pairs is the spontaneous parametric down-conversion (SPDC). In this non-linear optical process, one photon spontaneously splits into two other photons of lower energies [49]. In a bi-photon source, a laser with frequency ω_p pumps a nonlinear crystal (NLC) with second order susceptibility $\chi^{(2)}$. One of the photons can be absorbed and converted into an entangled pair of photons with frequencies ω_s (signal) and ω_i (idler) [50]. When the frequency of the signal and idler photons satisfy $\omega_s = \omega_i$ it is known as the degenerate case, otherwise it is not degenerated.

The trajectory of the emitted photons, i. e. the angle of emission, is determined by the conservation of energy (phase matching) $\omega_p = \omega_s + \omega_i$, see Fig. 2.7. The signal and idler

photons' emission can be collinear or noncollinear; if the emission angle is zero, then the photons are collinear.

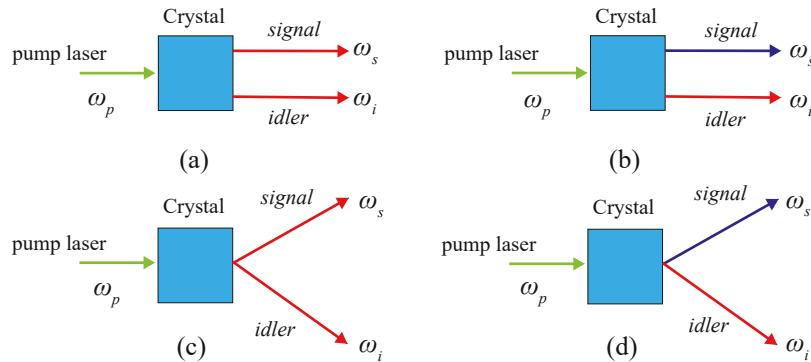


Figure 2.7: Bi-photon source. A pump photon of frequency ω_p propagating inside a nonlinear crystal is spontaneously down-converted in two photons of frequency ω_s and ω_i . The photon pair generation is (a) collinear with degenerate photons ($\omega_s = \omega_i$), (b) collinear with nondegenerate photons ($\omega_s \neq \omega_i$), (c) noncollinear with degenerate photons, and (d) noncollinear with nondegenerate photons.

Some common nonlinear crystals used for SPDC are KDP (potassium dideuterium phosphate, KD_2PO_4), BBO (beta barium borate, BaB_2O_4), LiNbO_3 (lithium niobate), and LiIO_3 (lithium iodate). According to the crystals, photons can be generated with entanglement in time, frequency, space, momentum, or polarization. The crystals can be classified into types 0, I and II. Type-0 crystals generate photons with the same polarization of the pump beam [51, 52], type-I generates time-frequency entangled photon pairs (signal and idler) with perpendicular polarization to the pumping beam [53, 54] and type-II emits polarized entangled photon pairs with crossed polarization [55, 56].

Comparing the structure of the OCT setup in Fig. 2.2, the bi-photon source takes the role of generating a photon for reference and another to interact with the sample. The architecture of the optical array used for photon interference leads to the use of non-linear interferometers as described below.

2.2.2 Nonlinear interferometers

Nonlinear interferometers are those in which a nonlinear optical effect takes place and emerges from the beginning of nonlinear optics. The last few years have seen a surge of interest in using these interferometers for new schemes in imaging [32, 57, 58], sensing [59, 60, 61, 62], spectroscopy [63, 64], microscopy [65, 66], optical coherence tomography [67, 68, 69, 70] and quantum detection [47, 71]. The nonlinear interferometers have architectures similar to a Michelson, Mach-Zehnder, and Hong-Ou-Mandel interferometer.

Photon interferometry conform experimental techniques for fast and sensitive measurement of light. The pioneer works of Mandel *et al.* uses a nonlinear type Mach-Zehnder interferometer to study the second-order interference observing the induced coherence effect

[28]. The measurement of the fourth-order interference in a Hong-Ou-Mandel nonlinear interferometer allows to observe the two-photon interference and describe the Hong-Ou-Mandel effect [72].

2.2.3 Induced coherence effect

The induced coherence effect is *the second-order interference of two-photon signal from two coherently pumped down-converters, when the paths of the idler photons are aligned* [28]. Figure 5.1 shows the original scheme of an induced coherence experiment based on a nonlinear Mach-Zehnder interferometer. Here, the first bi-photon source generates signal s_1 and idler i_1 photons. The photons s_1 travel to a reference mirror and i_1 to the second down-converter crystal generating a second pair of photons s_2 and i_2 . The injection of i_1 into the second nonlinear crystal induces coherence between signal photons s_1 and s_2 . After the beamsplitter, the detector D_s measures the interference between s_1 and s_2 . Zou *et al.* discovers that the visibility of the interference varies if the photons i_1 are blocked, putting a filter between the nonlinear crystals, i. e., the transmissivity change as they report in curves A and B of Fig. 5.1. On the other hand, when the beamsplitter moves, the visibility of the interference change. This effect has a parallelism with the interference in an OCT system where a multi-layer sample replaces the filter NDF. Instead of moving the BS_0 , the reference mirror (M_1) moves as in TD-OCT system of Fig 2.2.

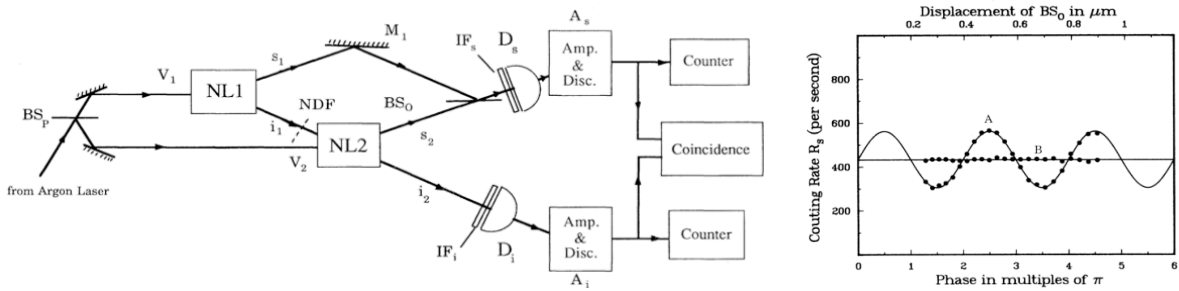


Figure 2.8: Nonlinear Mach-Zehnder interferometer with two bi-photon sources to study the induce coherence effect [28]. The interference of photons s_1 and s_2 depends on the transmissivity of the filter NDF. The visibility of the interference varies periodically, moving the beamsplitter. Curve A: filter with a transmissivity of 0.91. Curve B: filter with a transmissivity of 0.

Notice that the idler photons i_1 from the first crystal are the ones that interact with the filter NDF. Nevertheless, the information is measured detecting the interference between the signal photons s_1 and s_2 . For this reason, the induced coherence effect is the basis for imaging with undetected photons.

The experiment changes if the signal s_1 and i_1 photons are injected into the second nonlinear crystal. This experiment is the case for an SU(1,1) interferometer that we present in chapter 4. Let us describe the Hong-Ou-Mandel effect as the second mechanism for quantum-based OCT systems.

2.2.4 Hong-Ou-Mandel effect

The Hong-Ou-Mandel effect is a consequence of the indistinguishability of two photons [26]. Figure 2.9 shows the original setup used by Hong *et al.* to study the photon timing between two photons and demonstrate experimentally the Hong-Ou-Mandel effect [72]. Here a bi-photon source emits entangled photon pairs of frequencies ω_1 and ω_2 directed to the beam-splitter BS. The photons enter on two separate input ports of the BS where the two-photon interference generating four scenarios:

- Photon of ω_1 is transmitted while ω_2 is reflected
- Photon of ω_2 is transmitted while ω_1 is reflected
- Both photons are transmitted
- Both photons are reflected

The two-photon interference generates the Hong-Ou-Mandel effect due to the indistinguishable photons when both photons enter the BS simultaneously and exit from one side.

Figure 2.9 shows the dependence of photon interference. In the first points, photons have a phase difference given by a delay. The photons do not enter simultaneously in the BS. Therefore, the photons exit from different faces of the BS traveling to the detectors D1 and D2 matching a photon coincidence. The delay reduces moving the BS, increasing the probability that both photons out for the same port. At the deep point, both photons travel to D1 or D2; therefore, the photon coincidence is null.

The Hong-Ou-Mandel experiment is the most applied arrangement in two-photon interference and gives a criterion for testing the degree of entanglement of two-photons with a wide range of applications in quantum science and technologies [73, 74, 75, 76].

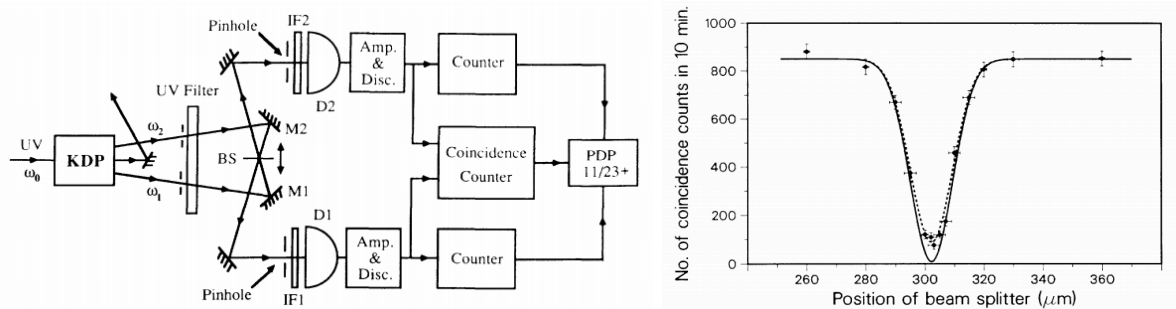


Figure 2.9: Hong-Ou-Mandel interferometer to study the two-photon interference [72]. Inducing a time delay moving the beamsplitter (BS), the detection of photon coincidences measures the photon interference giving a minimum (HOM deep) when the optical paths are equal.

2.3 Summary

In this chapter, we analyze how OCT facilitates optical depth sectioning. This technique is advantageous in materials with a layered structure, mainly biological materials. The OCT

technique developed by Fujimoto *et al.* is ideal for applications that demand resolutions of micrometers and even sub-micrometer. The fast image acquisition is a tremendous advantage for applications in real-time medical diagnosis.

We study the principles of OCT in the Temporal and Fourier domain. The architecture of their optical setups is very similar, but the TD-OCT systems have movable parts while FD-OCT does not, see Fig. 2.2. This difference transforms image acquisition. TD-OCT performs a scan to measure the interferogram of the sample that gives the information of the optical distance between layers. On the other hand, the FD-OCT captures the modulated spectrum and, its Fourier transform reveals the information of the sample structure. In a way, it is more complex to interpret an FD-OCT image than a TD-OCT, as shown in Figs. 2.4 and 2.5.

OCT has demonstrated exceptional performance; however, the demand for increasingly precise systems encourages new developments. The challenge is to eliminate the effects that distort images, such as chromatic dispersion or low resolution. In efforts to achieve this, a potential solution is found by harnessing the quantum properties of light. This solution is possible by developing new OCT systems considering non-classical light sources, nonlinear interferometers, and singular photon detection systems.

OCT based on quantum principles transforms the physics of the classical technique. These systems work with the interference of individual photons taking advantage of the photon entanglement. The vast majority of the methods carried out use photon pairs generated by SPDC in nonlinear crystals. The downside is that the SPDC process is super inefficient, and the generation of photon pairs is inadequate for practical applications. On the other hand, nonlinear interferometers have been widely developed and offer a basis for quantum imaging. In particular, Mandel *et al.* used them to study the induced coherence between two independent photon-pair sources. Also, they worked on the indistinguishability of entangled photon pairs known as the Hong-Ou-Mandel effect. These two studies demonstrated the second and fourth-order interference of photon pairs which are the fundamentals of the quantum-based OCT systems.

Chapter 3

Photon counting and timing using an oscilloscope

Quantum-based OCT systems use bi-photon sources and single-photon detection for photon counting and timing. One of the main components for this task is the photon timer. This chapter develops a method for photon counting and timing using an oscilloscope, a low-cost solution compared to the commercials. Our test compares the temporal correlations between a source of time-correlated photons and another of time-uncorrelated photons. The former is an entangled twin-photon source, and the latter is an attenuated light beam from a diode laser. We characterize the light sources by measuring the histogram of coincidences and the Joint Current Rate (JCR). At the end of the chapter, we understand how the simplicity of this methodology proposes an innovative application of oscilloscopes in quantum interference.

3.1 Introduction

Photon counting and timing are generic tasks in many photonics laboratories to measure single-photon interference. Single-photon detection is used in second-order interference measurements to study the phenomenon of induced coherence [28]. Fourth-order interference is used in Hong-Ou-Mandel experiments to measure the photon pair coincidences [15]. For such experiments, a twin-photon source and a photon counter system are central components.

A twin-photon source is constructed by pumping a non-linear crystal with a laser beam, generating entangled photons through the SPCD process. The development of photon-pair sources is of great interest to quantum communications [77, 78, 79], quantum computing [80, 81], and quantum imaging [34, 82, 83]. It seeks to develop photon sources that generate a high rate of photon emission (brightness) on different platforms such as crystals [84, 85, 51], waveguides [86, 87] or quantum dots [88, 19].

At the undergraduate level, there is interest in teaching basic quantum optics experiments such as photon interference, correlations, polarization, and entanglement [89, 90, 91, 92, 93]. The Mandel interferometer allows studying the two-photon interference measuring the photon coincidences [15]. The photon coincidence is the simultaneous detection of single photons in two or more detectors, for such a task is indispensable a coincidence counter device [90, 91]. The commercial coincidence counters has time precision of 4ps [94] and 14ps [95] but have a

relatively high cost. Homemade low-cost coincidence counter units (CCU) are an alternative to commercial coincidence counters with time resolution in the order of nano seconds [96, 97, 98]. However, a CCU construction can be a tedious work if the main interest is not electronics.

In this chapter we demonstrate the use of an oscilloscope as a coincidence counter. The oscilloscope is a standard instrument for analyzing electrical signals used by STEM students in science laboratories. Modern digital oscilloscopes provide the advantage of saving the data for post-processing. Here, we develop a simple procedure to measure photon coincidences using a basic digital oscilloscope. Its everyday use makes it an easy-to-use tool for understanding the photon counting and timing.

3.2 Methodology

3.2.1 Twin-photon source

We construct a source of time-frequency entangled photon pairs, our pump beam is a diode laser (CrystaLaser BCL-300-405) with a spectrum that ranges between 349 – 501 nm, as shown in Fig. 3.1. Its horizontal polarization is selected using a polarizing beamsplitter (PBS) and filtered with a narrower bandpass filter (NewLight NBF405-10) centered at 405 ± 5 nm.

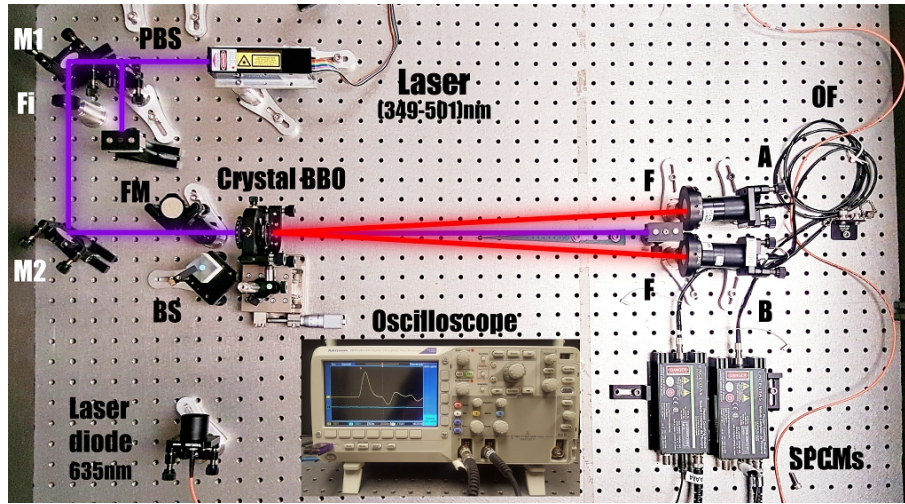


Figure 3.1: Experimental setup of an entangled twin-photon source. Here the photons of wavelength centered at 405 nm are transformed in two of 810 nm. The components are a polarizing beamsplitter (PBS), mirrors (M1 and M2), filter at 405 nm (Fi), beamsplitter (BS), a flip mirror (FM), Type I BBO crystal, linear polarizer, filters at 780 nm and (810 ± 5) nm (F), collectors (A and B), multimode fibers (OF) and single-photon counting modules (SPCMs) and an oscilloscope for photo timing.

The laser beam with a wavelength $\lambda_p = 405 \pm 5$ nm pumps a beta barium borate crystal (BBO, type I) generating signal and idler photons with a central wavelength of 810 nm and are emitted with a cone angle of 6° . The emitted photons have perpendicular polarization to the pumping beam. We 3D printed a wedge with an aperture of 6° to position irises (not shown in Figure 3.1) for the alignment of photon collectors A and B.

A photon collector consists of fiber coupling optics, an aspheric lens (Thorlabs C220TME-B), and a fiber connector (Thorlabs SM1FC), both inserted in a tube lens which is mounted in a kinematic mount for transverse alignment (Thorlabs KM100T). The focus of the lens is adjusted with a spanner wrench. Before the fiber collection stages, we put a linear polarizer (Thorlabs, LPNIRE100-B) vertically oriented, a 780 nm long-pass filter (Thorlabs, FGL780), and a narrow bandpass filter centered at 810 ± 5 nm (NBF810-10 from Newlight Photonics) to ensure the spectral quality and polarization of the photon pairs.

The flip mirror behind the crystal allows the align the light from the diode laser, see Fig. 3.1. The beamsplitter is placed so that both light beams generated have the same path as the pair of entangled photons when the flip mirror rises.

3.2.2 Single photon detection

The photons from the bi-photon source are coupling in multimode fibers with a length of 1 m (Thorlabs, model M31L01) connected to fiber-coupled avalanche photodetectors (Excelitas, SPCM-AQRH) with a photon detection efficiency of 60% at 810 nm, dark counts of 150 counts per second and a transistor-transistor logic (TTL) output pulse width of 10 ± 2 ns. The fibers are covered with black tape to reduce the background illumination.

The photodetectors outputs are fed into input channels A and B of the oscilloscope (Tektronix DPO 2012B). The oscilloscope monitors pulse trains. Figure 3.2 shows the wavefront of a pulse of 10 ns at the FWHM.

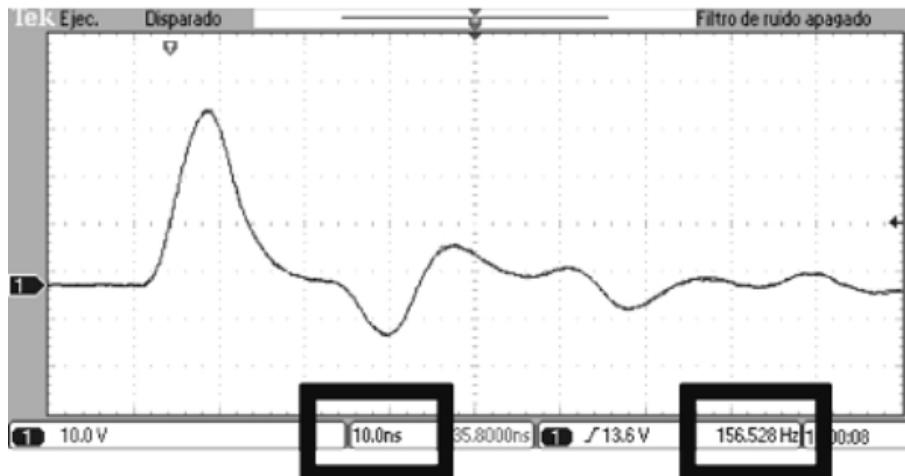


Figure 3.2: Oscilloscope wavefront of a transistor-transistor logic (TTL) output pulse with time scale (10 ns/div) and frequency (156 Hz). The pulse has a width of 10 ± 2 ns and the side oscillations are attributed to partial reflections from the electrical connections.

The oscilloscope has a maximum sampling rate of 1 Gs/s (giga sample per second), which results in a time resolution of 1 ns. Figure 3.2 shows a pulse coming from the photodetectors' dark counts (i.e., without detecting light). Notice that the pulse waist is approximate 10 ns at the FWHM. The small oscillations are attributed to reflections coming from the electrical connections (these oscillations are observed even when we use the 50Ω required for impedance matching). The frequency displayed is approximately 156 Hz, which is at the

level of the photodetector dark counts per second. Therefore, frequency is equal to the single counts per second.

The oscilloscope captures pulse trains composed by the detectors dark counts, time-correlated and time-uncorrelated photons. Before experimentation, we make a simulation of data acquisition and processing.

3.2.3 Simulation of photon coincidences

The histogram of coincidences is a graphical representation of the arrival time difference between the signal and idler photons. The statistics of the photon coincidences allow distinguishing between time-correlated and time-uncorrelated photons. Consider the pulse trains in Fig. 3.3(a). The number "1" represents the peak of a pulse and "0" the other points. The position of each pulse is assigned using a pseudo-random integer generator with a uniform distribution. Each pulse has the same temporal position in both arrays for time-correlated photons, and time-uncorrelated photons have a random position.

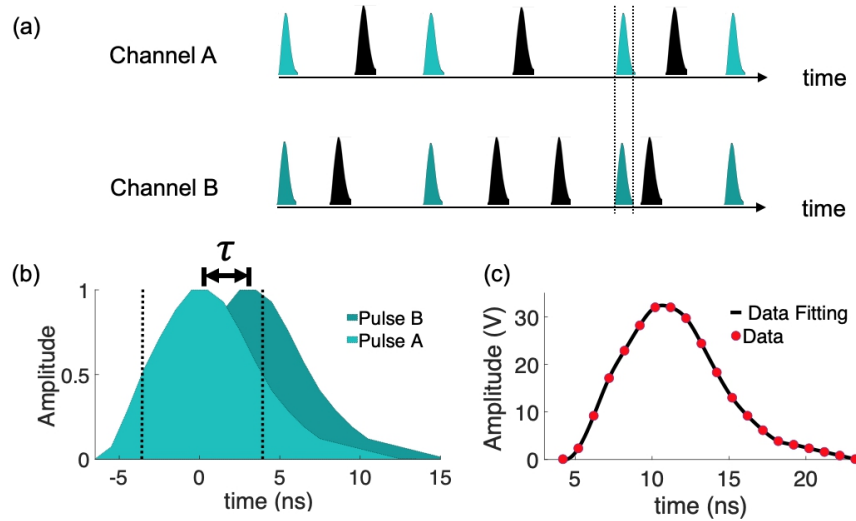


Figure 3.3: (a) Modeling of the pulse trains of single photons. (b) Time window (τ) for photon counting the photon pairs. (c) Pulse detection with resolution of 1 ns (dot) and its interpolation to achieve a resolution of 5 ps (line).

Photon coincidence counting relies on measuring the time difference between pulses (τ) from channels A and B, see Fig. 3.3(b). Pulses with a time difference less than τ count as a photon coincidence [92, 97]. Figure 3.4(a) presents the simulation of photon coincidences considering an array of 33 time-correlated photons, and 24000 time-uncorrelated photons distributed in a time of 100 ms with a resolution of 1 ns. It presents a peak of 41 coincidences and an average background of 10 accidental coincidences. Therefore, the number of coincidences is 31, consistent with time-correlated photons' input value. In Fig. 3.4(b), we show the simulation without considering time-correlated photons. The peak of coincidences disappears, and the average background remains at 10.

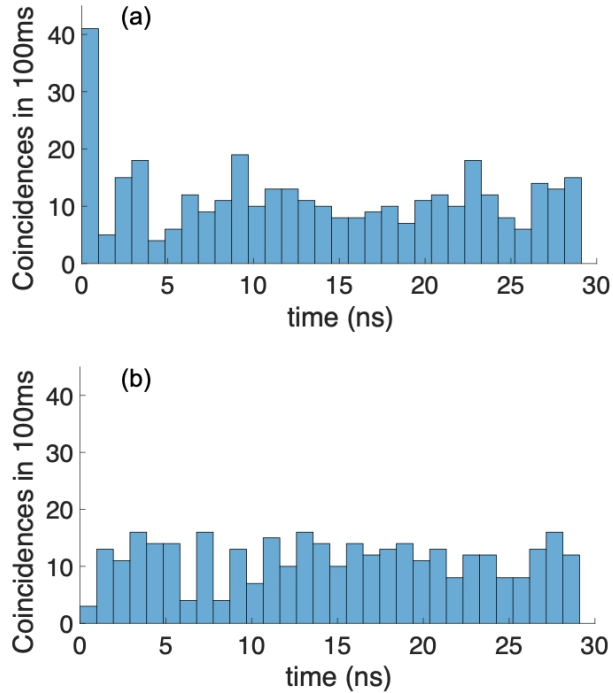


Figure 3.4: Simulation of the histogram of coincidences with bin size of 1 ns for (a) time-correlated photons and (b) time-uncorrelated photons.

Simulations in Fig. 3.4 demonstrate the procedure to measure photon coincidences using the oscilloscope signals. The oscilloscope works with time windows, as presented in Fig. 3.2. For a time window of 100 μs and a resolution of 1 ns, the recording time is approximately 38 s. An acquisition time of 100 ms needs 1000 captures equivalent to a recording time of 38000 s. We automatize the photon detection system for the experimental measurement. The MATLAB codes for simulating photon trains, oscilloscope automating, and data processing can be download from [99, 100, 101].

3.3 Experimental results

3.3.1 Photon coincidences

For a pump beam power of $P = 29$ mW, the emission of entangled photons is 210k photons per second (210 kHz). Figure 3.5(a) shows the histogram of coincidences with a peak of 32 coincidences with an average background of 3 accidental coincidences. Working with the light from the attenuated red laser, the peak of coincidences disappears remains the background of accidental coincidences, see Fig. 3.5(b).

The measurement of the histogram of coincidences in Fig. 6 shows the difference between classical and non-classical light sources. The peak of coincidences in Fig. 3.5(a) near zero means that time-correlated photons from A and B arrive simultaneously, i. e., the photons optical paths are equal. If one optical path is longer, the time-correlated photons' timing has

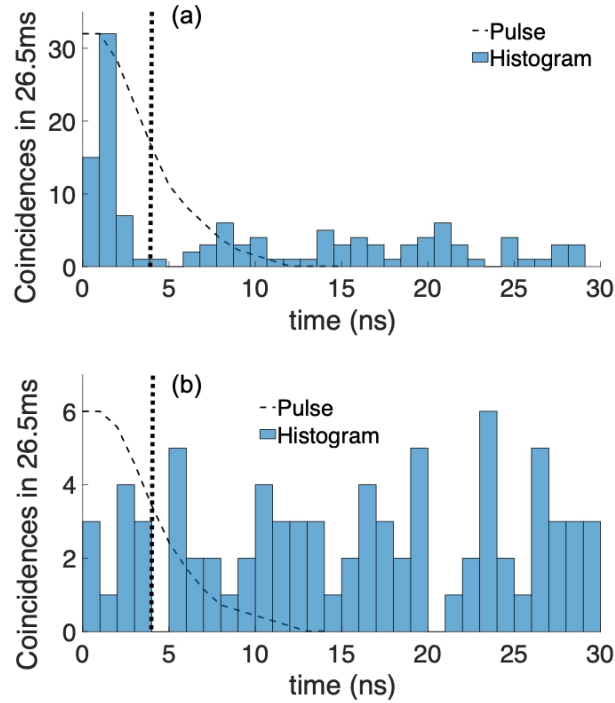


Figure 3.5: Measurement of the histogram of coincidences with bin size of (a) time-correlated photons, and (b) time-uncorrelated photons.

a delay given by the difference in the optical paths.

3.3.2 Optical path photon delay

Adding 2.0 m of optical fiber in channel B, we study the effect of photon delay in the histogram of coincidences. The optical fiber (Thorlabs, M31L01) has a refractive index of 1.487; therefore, the delay is 9.9 ns. For a $P = 34.1$ mW pump power, the frequency in channel A is 245 kHz, and in channel B is 174 kHz. The difference in single counts are losses for the additional fiber connectors in channel B. Figure 3.6(a) shows the histogram of coincidences with a peak of 30 coincidences shifted around 10 and 11 ns. Comparing the figures Fig. 3.5 (a) and Fig. 3.6 (a) the delay is between 9 and 10 ns, close to the expected value.

The resolution in the histogram of coincidences can be enhanced by fitting the experimental data using spline interpolation, as is presented in Fig. 3.3 (c). Figure 3.6(b) shows the histogram of coincidences with a resolution of 5 ps with the peak of coincidences at 10.705 ns. Therefore, the time delay is $t_d = 9.75$ ns closest to 9.9 ns, which is the expected value. The photon timing precision is comparable with the most advanced commercial coincidence counters of 4 ps and 14 ps.

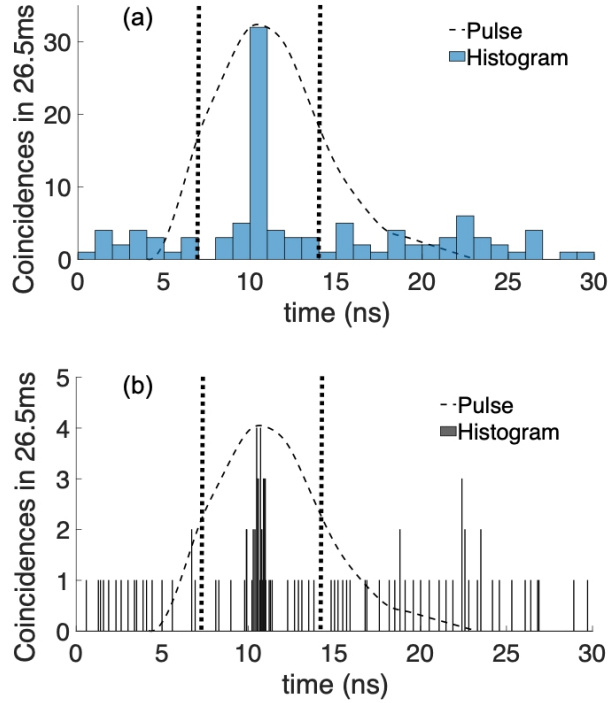


Figure 3.6: Delay effect in the histogram of coincidences of time-correlated photons with (a) Bin size of 1 ns from experimental data and (b) Bin size of 5 ps from experimental data fitting. The pulse duration defines the broadest coincidence time windows. The pulse resolution is 1 ns and 5 ps respectively.

3.3.3 Joint current rate

The joint current rate (JCR) is defined as the brightness ($\frac{\# \text{ pairs}}{s}$) per pump power in mW, written as

$$JCR = \frac{\# \text{ photon pairs}}{s \text{ mW}} \quad (3.1)$$

Table 3.1 presents the dependence of coincidence measurements on the pump power.

P (mW)	F (kHz)	$\frac{\# \text{ photon pairs}}{s}$	JCR
7.5	60	189	25.2
12.8	100	302	23.59
18.2	150	491	26.97
23.7	186	1509	63.67
29	210	1208	41.65

Table 3.1: Coincidence measurements in function of the pump power. P is the pump power, F frequency and JCR joint current rate.

The coincidences increase as the pump power increases, but it is clear that it is not a linear behavior. The ratio of photon pairs per single counts is between 0.5% to 0.8%, and the JCR is between 23 to 63. We know that strictly speaking, the waveforms from either

the dark counts or the down-converted photons are not periodic, which means that the frequency displayed by the oscilloscope is averaged (the becquerel (Bq) units would be a better description).

Ideally, the photon pair emission rate is linear to the intensity of the pump [48]. In our case, however, the coincidences increase as the pump power increases but not with a linear behavior. This could be because the crystal's refractive index depends on the pump intensity, which changes the phase-matching condition and, therefore, the down-converted photons' spectrum and emission angle. For a better measurement, it is necessary to realign the collectors for each pump power. Furthermore, the ratio of pairs per single counts seems to be low (our best is close to 0.8%). We ascribe this low ratio to our fiber coupling systems, limiting the 2 axis.

3.4 Conclusions

We develop a simple photon counting and timing method using a digital oscilloscope as a photon timer. This simple methodology proposes an innovative application of oscilloscopes in quantum optics experiments, such as the characterization of an entangled twin-photon source.

The measurement of the histogram of coincidences allows comparing the statistics of time-correlated photons from a bi-photon source with the statistics of time-uncorrelated photons from an attenuated light beam. The histogram of coincidences presents the typical peak of coincidences. We achieved time resolutions of 5 ps in the coincidence histogram, comparable with the most advanced commercial coincidence counters.

Additionally, we study the displacement of the histogram of coincidences inducing a photon delay by the propagation through a longer optical fiber. This effect is used to get information about photon path propagation. The time delay measurement is crucial in optical depth sectioning techniques, such as in the Time-Domain Optical Coherence Tomography and its quantum versions, as we present in chapter 4.

We remark that this strategy's disadvantage is not the time resolution measurements but the long recording time, limiting its application in experiments that require several acquisitions. Its primary potential application is education because modern digital oscilloscopes are available in most universities and are more familiar for students, technicians, professors, etc.

Chapter 4

OCT based on nonlinear interferometers

The new techniques for optical depth sectioning based on quantum principles impulse the quantum technologies. These technologies inspired by OCT take advantage of the quantum correlations between down-converted photons to enhance the image resolution. This chapter analyzes the techniques of induced coherence tomography (ICT), OCT in a $SU(1,1)$ interferometer, and quantum-OCT based on nonlinear interferometers and compares their performance with the standard FD-OCT scheme. We deduce analytical expressions with a homogeneous notation for all techniques allowing an easier study. As a study case, we analyze a bi-layer sample getting its spectrogram for each technique and recover the sample's depth information through the Fourier transform. Finally, we explore the contrast between layers depending on the reference mirror's reflectivity in the interferometer. At the end of the chapter, we understand the principles of operation and the image interpretation for each technique.

4.1 Introduction

The Fourier domain optical coherence tomography (FD-OCT) is the evolution of the Time domain-OCT (presented in chapter 1). In the Fourier domain, the principal advantage is faster testing of the sample. Advances on optical coherence tomography based on nonlinear interferometers have appeared in recent years: induced coherence tomography (ICT) [68, 64], OCT using an $SU(1,1)$ interferometer [45, 102], and quantum-OCT (QOCT) [103, 104, 105]. ICT uses the notion of induced coherence between two pairs of down-converted photons (signal and idler). A down-converter consists of a nonlinear crystal pumped by a laser. In this method, one of the idler photons reflects from a layered sample before being merged with the idler mode of the second down-converter. This modifies the first-order correlation function between the signal photons, providing information about the internal structure of the sample [68].

An $SU(1,1)$ interferometer is a variation of an induce coherence experiment where, in addition to the idler photons, the signal photon of the first down-converter is also recombined with the signal mode of the second crystal. This type of interferometer can also be used for OCT with practical advantages such as higher photon fluxes and better signal-to-noise ratio [45].

The previous schemes consider the first-order correlation function between the signal

modes. Instead, QOCT makes use of the second-order correlation function [30]. QOCT relies on the Hong-Ou-Mandel (HOM) effect. Here, two photons enter simultaneously through two input ports of a beam splitter, a coincidence dip is observed if both photons are indistinguishable. If one of the photons carries the information of the sample, the coincidence interferogram shows a HOM dip for each layer of the sample which are separated accordingly to the optical path-length difference between the layers. QOCT offers resolution enhancement and dispersion cancellation [30, 29, 106, 107]. This method has regained attention due to recent advances in photodetection technologies and down-converter crystals.

Valles *et al.* works with TD-OCT in an induced coherence scheme studying a sample with two layers separated 1 mm apart [68]. Machado *et al.* probes a $d = 100 \mu\text{m}$ thick microscope glass slide using a FD-OCT with an SU(1,1) interferometer [45]. On the other hand, Yepiz-Graciano *et al.* analyses a sample of borosilicate glass coverslip of $d = 170 \mu\text{m}$ thickness using a hybrid system for TD-QOCT and FD-QOCT [104]. The previous experimental methods have been implemented in samples such as glass slabs where the refractive index changes allow the optical contrast between layers.

With the recent increase in the potential implementation of the OCT-based on quantum techniques, users and companies need to know the performance and image interpretation between methods. This chapter describes the Fourier domain OCT based on quantum interferometry and compares their performance with the classical OCT configuration. To do this, we derive practical expressions for the output spectrum considering an exemplary two-layer sample.

4.2 OCT in a SU(1,1) interferometer

OCT in a SU (1,1) interferometer is a technique based on the effect of induced coherence, which allows the capture of images with undetected photons [32]. This means that it uses photons with the most appropriate wavelength to analyze the sample, but the image is captured with light of the wavelength that allows the best detection efficiency in the detector. By capturing the image with the best detection efficiency, the exposure time will be shorter and therefore the image acquisition time will be the shortest.

Figure 4.1 shows the schematic to realize FD-OCT with a SU(1,1) interferometer. A parametric down-converter generates entangled signal (s_1) and idler (i_1) photons with frequencies $\omega_{s_1} = \omega_s + \Omega$ and $\omega_{i_1} = \omega_i - \Omega$. A dichroic mirror separates the pump beam and signal photons from the idler photons. The pump and signal photons travel to the reference arm of length z_1 , while the idler photons toward the sample arm of length z_2 . The reference mirror reflects the pump and signal photons to the nonlinear crystal. Similarly, the sample reflects the idler photons to the nonlinear crystal. The second pass of the pump through the nonlinear crystal and the injection of s_1 and i_1 generate two new entangled photons s_2 and i_2 , where the signal photon s_2 is sent to the detection point.

The spectrum of the interference between photons s_1 and s_2 is described by [45]

$$S(k)_{\text{SU}(1,1)} = |V_s(k)|^2 [1 - |r_i(-k)|^2] + |r_R U_s(k) \exp[i\varphi_s(k)] + r_i^*(-k) U_i^*(-k) \exp[-i\varphi_i(-k)]|^2, \quad (4.1)$$

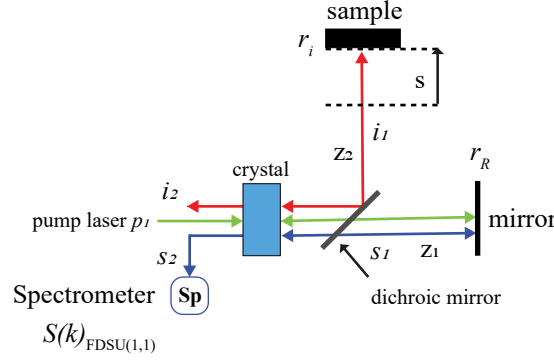


Figure 4.1: Fourier domain OCT with a SU(1,1) interferometer scheme. Here, a laser pumps the nonlinear crystal generating a pair of entangled photons: signal (s_1) and idler (i_1). The dichroic mirror separates the pump, signal, and idler photons. The photons are reflected, and after the second pass of the pump through the nonlinear crystal, the new signal photons s_2 are correlated with the first ones detected by the spectrometer Sp.

with

$$U_{s,i}(k) = \left\{ \cosh(\Gamma L) - i \frac{\Delta_{s,i}}{2\Gamma} \sinh(\Gamma L) \right\} \exp \left\{ i [k_p + k_{s,i}(k) - k_{i,s}(-k)] \frac{L}{2} \right\}, \quad (4.2)$$

$$V_s(k) = -i \frac{\sigma}{\Gamma} \sinh(\Gamma L) \exp \left\{ i [k_p + k_s(k) - k_i(-k)] \frac{L}{2} \right\}. \quad (4.3)$$

Here, $k = \Omega/c$ where Ω designates the frequency deviation from the central frequencies $\omega_{s,i}^0$ with $k_{s,i}^0 = \omega_{s,i}^0/c$ (i.e. $k_{s,i} = k_{s,i}^0 + k$), the phases are $\varphi_{s,i}(k) = k_{s,i} z_{1,2}$ and $z_{1,2}$ are the optical paths traversed by the signal and idler photons. The subscripts s,i refer to the signal and idler beams, $\Gamma = (\sigma^2 - \Delta_s^2/4)^{1/2}$ and the phase-matching functions are $\Delta_s = -\Delta_i = (D_i - D_s)\Omega$. $D_{s,i}$ are inverse group velocities at the signal and idler central frequencies, respectively. The nonlinear coefficient σ is

$$\sigma = \left(\frac{\hbar k_p^0 k_s^0 k_i^0 [\chi^{(2)}]^2 R_p}{8\epsilon_0 A n_p n_s n_i} \right)^{1/2}, \quad (4.4)$$

where $n_{p,s,i}$ are the refractive indices for the pump, signal and idler frequencies, respectively. A is the effective area of interaction and R_p is the flux rate of pump photons. We estimate R_p as $R_p = E_p/(\hbar\omega_p)/T_0$ where T_0 is the pump pulse duration, and E_p is the energy per pump pulse. r_R is the reflection coefficient of the reference mirror and $r_i(k)$ is the transfer function of the sample.

In the low-parametric gain regime, $U_{s,i}$ and V_s becomes

$$\begin{aligned} U_s(k) &= \exp [ik_s(k)L] = \exp [ik_s^0 n_s L + icD_s k L], \\ U_i(k) &= \exp [ik_i(k)L] = \exp [ik_i^0 n_i L + icD_i k L], \\ |V_s(k)|^2 &= (\sigma L)^2 \text{sinc}^2 \left(\frac{cDLk}{2} \right). \end{aligned} \quad (4.5)$$

The phase terms $U_{s,i}$ are given by the effect of the crystal of length L and V_s is the

spectral shape from a down-converter. The phase terms $\varphi_s(k) = k_s z_1$ and $\varphi_i(k) = k_i z_2$ given by the eq. (4.1) are the optical paths z_1 and z_2 .

4.2.1 Spectrogram FD-OCT in a SU(1,1) interferometer

The spectrometer measures the sample's modulated spectrum $S(k)_{\text{FDSU}(1,1)}$ and the Fourier transform of the output spectrum $\mathcal{F}\{S(k)_{\text{FDSU}(1,1)}\}$ reveals the depth information of the sample.

Considering the model of a bi-layer sample $N=1$ in eq. (2.7), the transfer function is

$$r_i(k) = r_0 + r_1 \exp[2i(k_i n_{0,1} + k n_{g,1})d], \quad (4.6)$$

and substituting eqs. (4.2) and (4.3) in eq. (4.1), we find that the spectral density is

$$\begin{aligned} S(k)_{\text{FDSU}(1,1)} = & (1 + R_R) |V_s(k)|^2 \left\{ 1 + 2 \frac{\sqrt{R_R R_0}}{(1 + R_R)} \cos[\varphi_1 - k(2s + cDL)] \right. \\ & \left. + 2 \frac{\sqrt{R_R R_1}}{(1 + R_R)} \cos[\varphi_2 - k(2s + 2n_{g,1}d + cDL)] \right\}, \quad (4.7) \end{aligned}$$

where $R_{R,0,1} = |r_{R,0,1}|^2$ and

$$\begin{aligned} \varphi_1 &= k_s^0 n_s L + k_i^0 n_i L + 2k_s^0 z_1 + 2k_i^0 z_2, \\ \varphi_2 &= k_s^0 n_s L + k_i^0 n_i L + 2k_s^0 z_1 + 2k_i^0 z_2 + k_i^0 2n_{0,1}d. \end{aligned}$$

It can be seen that Eq. (4.7) is a sum of three terms. Besides a constant offset (the self-interference term), the last two terms (the cross-interference terms) encode the depth information of the sample. Moreover, the amplitude of the cosine terms is proportional to the reflectance of the layers. As in FD-OCT, the Fourier transformation of $S(k)$ gives the sample's depth information. The Fourier transform of $S(k)_{\text{FDSU}(1,1)}$ is equal to

$$\begin{aligned} \hat{S}(z)_{\text{FDSU}(1,1)} = & (1 + R_R) \left\{ \hat{V}_s(z) + \frac{\sqrt{R_R R_0}}{(1 + R_R)} \exp(i\varphi_1) \hat{V}_s(z + (2s + cDL)) \right. \\ & \left. + \frac{\sqrt{R_R R_1}}{(1 + R_R)} \exp(i\varphi_2) \hat{V}_s(z + (2s + 2n_{g,1}d + cDL)) \right\} + c.c., \quad (4.8) \end{aligned}$$

where $\hat{V}_s(z)$ is the Fourier transform of $|V_s(k)|^2$. The Fourier-transformed spectrum shows five peaks. The central peak comes from the self-interference term. The cross-interference terms generate two peaks located at $z > 0$ and the conjugate peaks located at $z < 0$. Notice that the cross-interference peaks are separated by a distance $2n_{g,1}d$, from which we can extract the optical thickness of the sample.

If only the idler photon from the first down-converter in the SU(1,1) interferometer is injected into the second down-converter, the scheme turns into an induced coherence experiment. Machado *et al.* proposes to insert a quarter-wave plate (QWP) to change the polarization of signal beam s_1 . Idler beam i_1 would seed the parametric amplification process in the second pass through the nonlinear crystal transforming from SU(1,1) to ICT [45].

4.3 Induced Coherence Tomography

Induced coherence tomography (ICT) is a technique based on induced coherence for imaging with undetected photons analogous to OCT in a SU(1,1) interferometer. The scheme analyzed uses two separate down-converters, as schematically depicted in Fig. 4.2. The pump beam is divided in two (p_1 and p_2) by a beamsplitter (BS). Both beams travel to crystal 1 and crystal 2 to configure two bi-photon sources. The first bi-photon source generates signal (s_1) and idler

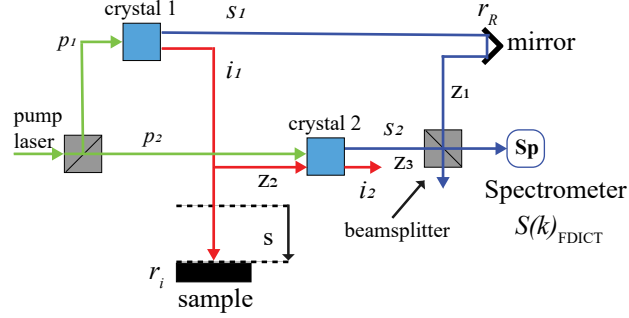


Figure 4.2: Fourier domain induced coherence tomography scheme in a type Mach Zehnder interferometer.

(i_1) photons with frequencies $\omega_{s_1} = \omega_s + \Omega$ and $\omega_{i_1} = \omega_i - \Omega$. The signal photons s_1 travel to the reference mirror. The idler photons i_1 travels to the sample and are reflected to entering the second down-converter crystal, which is being pumped coherently by p_2 . This generates a second pair of signal (s_2) and idler (i_2) photons. After the beamsplitter, the interference gives a measure of the coherence between photons s_1 and s_2 . From the eqs. (4.1) the spectrum is given by

$$S(k)_{\text{ICT}} = |V_s(k)|^2 \left\{ 1 - |r_i(-k)|^2 + \left| r_R \exp [ik_s^0(k)z_1] + r_i^*(-k)U_i^*(-k) \exp [-ik_i^0(-k)z_2 + ik_s^0(k)z_3] \right|^2 \right\}, \quad (4.9)$$

where $k_{s,i}^0(k) = k_{s,i} + k$ is the wavenumber in vacuum and $k_{s,i} = \omega_{s,i}/c$ and $k = \Omega/c$. Notice that U_s has not effect on eq. (4.9) and from eq. (4.5) $U_i(k) = \exp [ik_i^0 n_i L + icD_i k L]$.

In the Fourier domain-ICT scheme in Fig. 4.2, the sample and the reference mirror have fixed position where the distance s induce a phase difference to capture the spectrum $S(k)_{\text{FDICT}}$.

4.3.1 Spectrogram FD-ICT

Considering the transfer function in eq. (4.6) of a bi-layer sample and substituting in eq. (4.9), the spectrum $S(k)_{\text{FDICT}}$ is

$$\begin{aligned}
S(k)_{\text{FDICT}} &= (1 + R_R) |V_s(k)|^2 \left\{ 1 + 2 \frac{\sqrt{R_R R_0}}{(1 + R_R)} \cos[\varphi_1 - k(2s + cD_i L)] \right. \\
&\quad \left. + 2 \frac{\sqrt{R_R R_1}}{(1 + R_R)} \cos[\varphi_2 - k(2s + 2n_{g,1}d + cD_i L)] \right\} \quad (4.10) \\
\varphi_1 &= k_s^0 z_1 + k_i^0 n_i L + k_i^0 z_2 - k_s^0 z_3, \\
\varphi_2 &= k_s^0 z_1 + k_i^0 n_i L + k_i^0 z_2 - k_s^0 z_3 + k_i^0 2n_{0,1}d.
\end{aligned}$$

The eq. (4.10) is a sum of three terms, a constant offset (the self-interference term), and the last two terms (the cross-interference terms) encode the sample's depth information.

The Fourier transform is

$$\begin{aligned}
\hat{S}(z)_{\text{FDICT}} &= (1 + R_R) \left\{ \hat{V}_s(z) + \frac{\sqrt{R_R R_0}}{(1 + R_R)} \exp(i\varphi_1) \hat{V}_s(z + (2s + cD_i L)) \right. \\
&\quad \left. + \frac{\sqrt{R_R R_1}}{(1 + R_R)} \exp(i\varphi_2) \hat{V}_s(z + (2s + 2n_{g,1}d + cD_i L)) \right\} + c.c., \quad (4.11)
\end{aligned}$$

where $\hat{V}_s(z)$ is the Fourier transform of $|V_s(k)|^2$. The Fourier-transformed spectrum shows five peaks. Notice that the cross-interference peaks are separated by a distance $2n_{g,1}d$, from which we can extract the optical thickness of the sample.

4.4 Quantum OCT

Quantum optical coherence tomography (QOCT) is an imaging technique based on the Hong-Ou-Mandel Effect (HOM) with the advantages of acquiring images with better resolution and dispersion cancellation.

Figure 4.3 shows its schematic setup where a parametric down-converter generates a pair of non-collinear entangled photons signal (s_1) and idler (i_1) with frequencies $\omega_{s_1} = \omega_{i_1}$. The idler photons travel to the sample under study, and signal photons travel to the reference mirror. The photons are reflected and travel to the beamsplitter, where they interfere. Finally, the bi-photon spectrometer detects the photon coincidences given by the Joint Spectral Intensity (JSI) [104, 103]

$$S(k)_{\text{QOCT}} = \frac{1}{4} |V_s(k)|^2 |r_i(k) - r_i(-k) \exp(-4ik(z_2 - z_1))|^2, \quad (4.12)$$

with $k = \Omega/c$. Figure 4.3 shows the Fourier domain-QOCT scheme where the mirror is static and the phase induced by the distance s modulates the spectrum $S(k)_{\text{FDQOCT}}$ that carries the sample information.

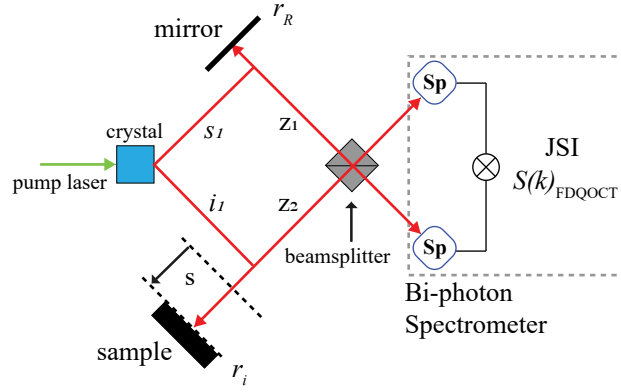


Figure 4.3: Fourier domain quantum-optical coherence tomography scheme in a Hong–Ou–Mandel interferometer. Here, a monochromatic laser of frequency ω_p pumps a nonlinear crystal (NLC) generating frequency entangled photons s_1 and s_2 . After the beam-splitter, the spectrogram $S(k)_{\text{FDQOCT}}$ is acquired by a bi-photon spectrometer.

4.4.1 Spectrogram FD-QOCT

Considering a bi-layer sample of transfer function in eq. (4.6) and substituting in eq. (4.12), the JSI is

$$\begin{aligned}
 S(k)_{\text{FDQOCT}} = & \frac{R_0 + R_1}{2} |V_s(k)|^2 \left\{ 1 + \frac{2\sqrt{R_0 R_1}}{R_0 + R_1} \cos(2k_0 n_{0,1} d) \cos(2n_{g,1} d k) \right. \\
 & - \frac{R_0}{R_0 + R_1} \cos(4s k) - \frac{2\sqrt{R_0 R_1}}{R_0 + R_1} \cos(2k_0 n_{0,1} d) \cos[(4s + 2n_{g,1} d) k] \\
 & \left. - \frac{R_1}{R_0 + R_1} \cos[(4s + 4n_{g,1} d) k] \right\}. \quad (4.13)
 \end{aligned}$$

with s the path difference. The Fourier transform is

$$\begin{aligned}
 \hat{S}(z)_{\text{FDQOCT}} = & \frac{R_0 + R_1}{2} \left\{ \hat{V}_s(z) + \frac{\sqrt{R_0 R_1}}{R_0 + R_1} \cos(2k_0 n_{0,1} d) \hat{V}_s(z + 2n_{g,1} d) \right. \\
 & - \frac{R_0}{R_0 + R_1} \frac{\hat{V}_s(z + 4s)}{2} - \frac{\sqrt{R_0 R_1}}{R_0 + R_1} \cos(2k_0 n_{0,1} d) \hat{V}_s(z + 2(2s + n_{g,1} d)) \\
 & \left. - \frac{R_1}{R_0 + R_1} \frac{\hat{V}_s(z + 4(s + n_{g,1} d))}{2} \right\} + c.c., \quad (4.14)
 \end{aligned}$$

where $z = 2\pi/k$ and $\hat{V}_s(z)$ is the Fourier transform of $|V_s(k)|^2$. The Fourier transform of the output spectrum features nine characteristic peaks, a central peak at $z = 0$, four located at $z > 0$ and four of them symmetrically located at $z < 0$, which are defined as the conjugated components and are denoted in Eq. (4.14) by c.c. There are three cross-interference peaks (s -dependent terms) which are separated among them a distance $2n_{g,1} d$. The peak located midway between the third and fifth term has amplitude that depends on the central spatial frequency k_0 and the properties of the sample ($n_{0,1}$ and d). Therefore, we can see that this term

can be either a peak or a dip depending on the sign of $\cos(2k_0n_{0,1}d)$ (it might also disappear if $2k_0n_{0,1}d$ is a multiple of $\pi/2$). This becomes important during the reconstruction process. If we want to recover the sample's thickness, it is recommended to use the peaks originating from the third and fifth terms, which are separated by a distance of $4n_{g,1}d$. Choosing these peaks, we are preventing the scenario where the intermediate peak disappears.

Let us now proceed with the simulation of the image acquisition for each technique including classical OCT from eq. (2.10) and eq. (2.12) to compare the images.

4.5 Results

For the simulation of classical OCT, we consider a light source with Gaussian spectral density described in Eq. (2.5) with central wavelength $\lambda_0 = 810 \text{ nm}$ and bandwidth of $\Delta\lambda = 10 \text{ nm}$. The spectral density in the nonclassical OCT is modeled with a sinc spectral shape written as

$$V(k) = \sigma L \text{sinc}\left(\frac{cDL}{2}k\right). \quad (4.15)$$

The coefficient σ is described in Eq. (4.4), L is the crystal length and $D = D_i - D_s$ with $D_{s,i}$ are the inverse of the group velocities of the signal and idler photons in the crystal. We consider photons with central wavelength at $\lambda = 810 \text{ nm}$ and bandwidth $\Delta\lambda = 10 \text{ nm}$, crystal length $L = 1 \text{ mm}$, $cDL = -79.1 \text{ }\mu\text{m}$ and $cD_iL = 2.2 \text{ mm}$ from a MgO-doped lithium niobate crystal. These values are congruent with the used for SU(1,1) interferometer and ICT of the references [68, 45]. Here a laser with central wavelength $\lambda_p = 532 \text{ nm}$ pumps a crystal generating signal photons of central wavelength $\lambda_s = 810 \text{ nm}$ and idler photons at $\lambda_i = 1550 \text{ nm}$. For QOCT the signal and idler photons are non-collinears with central wavelengths $\lambda_{s,i} = 810 \text{ nm}$ [108, 103, 104]. The spectral shape of the signal photons has a bandwidth of $\Delta\lambda = 10 \text{ nm}$.

The numerical simulations consider a bi-layer sample with thickness $d = 100 \text{ }\mu\text{m}$ and refractive index $n_{0,1} = n_{g,1} = 2.33$. Thus, the optical thickness is $n_{g,1} = 0.233 \text{ mm}$. Assuming the sample is immersed between air $n_{0,0} = n_{g,0} = 1$ and gel $n_{0,2} = n_{g,2} = 1.3$, the Fresnel coefficients are $R_0 = 0.16$ and $R_1 = 0.11$ for the first and second layers of the sample (R_2 takes into account the transmissions of the first interface). The reflection coefficient of the reference mirror is $r_R = 1$.

4.5.1 Fourier domain spectrograms

Figure 4.4 shows the output spectrum $S(k)$, and its Fourier transform $\hat{S}(z)$. From the first column, we can notice that the output spectrum is a highly oscillatory function with the oscillating frequency depending on the path length difference s . It is worth observing that for all methods, except QOCT, the output spectrum is an odd function of k , resulting in a complex Fourier transformation. The spectrum of FD-QOCT is an even function of k . Thus its Fourier transform is real.

The second column of Fig. 4.4 shows the absolute value of $\hat{S}(z)$ (we have chosen not to display the negative components on account of the symmetry of $|\hat{S}|$). We also indicate the separation of the cross-interference terms from the central peak to highlight the main

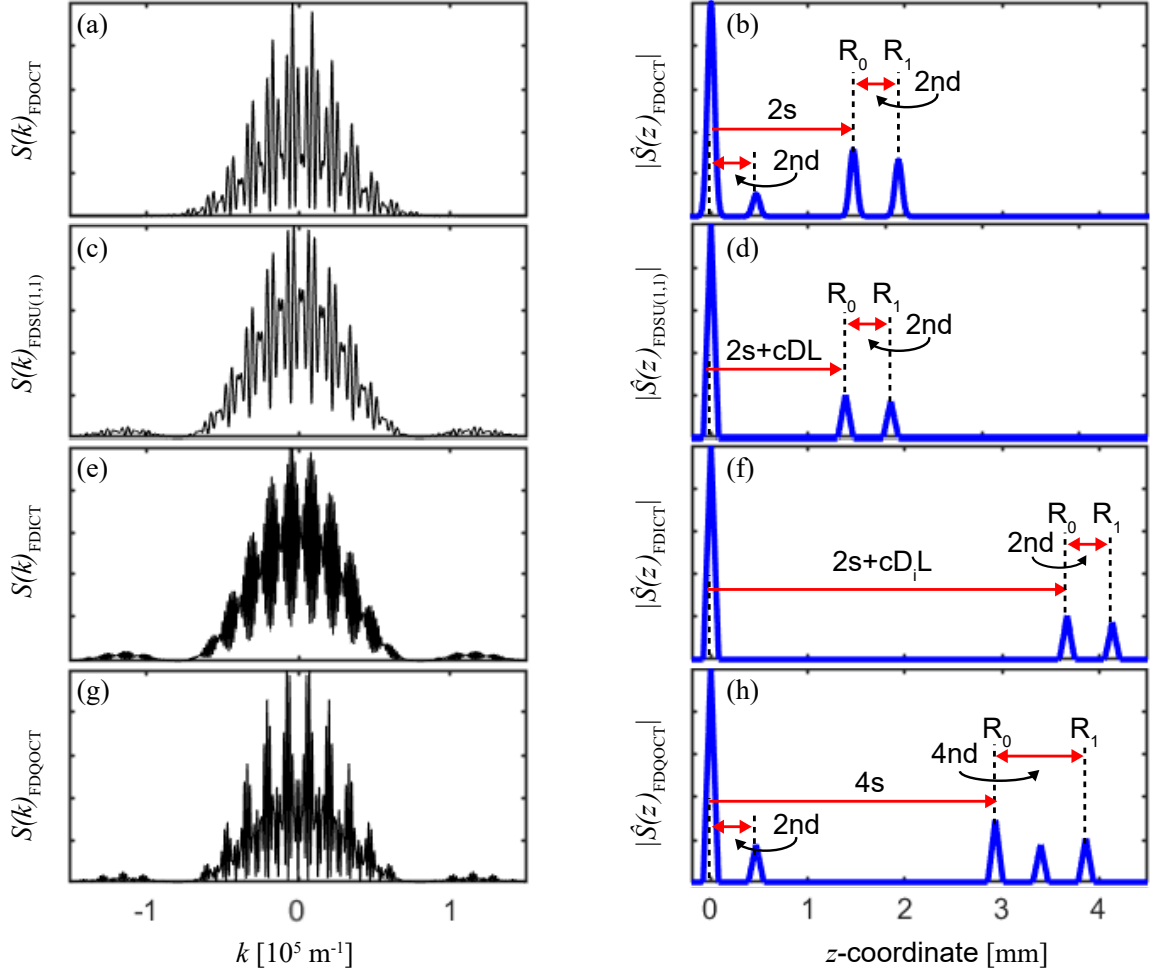


Figure 4.4: The left column shows the output spectrum $S(k = \Omega/c)$ for all the methods under study. The right column shows the Fourier transform of the spectrum. We only display the positive z -axis due to the symmetry of $|\hat{S}(z = 2\pi/k)|^2$.

differences between the methods. Both FD-SU(1,1) and FD-ICT show only two peaks derived from the cross-interference terms. These peaks are labeled as R_0 and R_1 since they come from the first and second layers, respectively. This is an advantage for image reconstruction since there is no room for misinterpretation of the results. On the other hand, in FD-OCT and FD-QOCT, the path-length difference s must be sufficiently large to isolate the cross-interference peaks from the side lobes of the self-interference terms. Another important observation is that the displacement of the cross-interference peaks also depends on the dispersion properties of the non-linear crystal used in the down-conversion process. For FD-SU(1,1), the displacement is $2s + cDL$, whereas for FD-ICT is $2s + cD_iL$. Therefore, these methods could be used in characterizing non-linear crystals [61].

To extract the optical thickness of the sample, in all methods, we can measure the separation between the peaks resulting from the cross-interference terms. In OCT, SU(1,1) and ICT, the separation is equal to $2n_gd$, whereas in QOCT is $4n_gd$ (from R_0 to R_1). The factor of 2 in QOCT is characteristic of the resolution enhancement provided by this method (cf. Ref.

[29]).

The last statement lets us address the question of the resolution conditions on the apparatus to appropriately sampling the spectrum. It is evident that s should be sufficiently large to isolate the cross-interference terms from the self-interference terms. But, the spectrometer's resolution should be small enough to sample the oscillations of the spectrum (as shown by the first column of Fig. 4.4). By noticing that the fringe separation in spatial frequency, $2\pi/s$, needs to be smaller than the bandwidth Δk of the spectrum and more extensive than the resolution δk of the spectrometer, and making use of $\delta k = 2\pi\delta\lambda/\lambda_0^2$ and $\Delta k = 2\pi\Delta\lambda/\lambda_0^2$, we arrive at the conclusion that s is constrained by

$$\frac{\lambda_s^2}{\Delta\lambda_s} \ll |s| \ll \frac{\lambda_s^2}{\delta\lambda}. \quad (4.16)$$

In our simulations, the path-length difference $s = 730 \mu\text{m}$ with a resolution of $\delta\lambda = 0.033 \text{ nm}$, therefore $0.065\text{mm} \ll |s| \ll 19.88\text{mm}$.

4.5.2 Interface contrast

From the analytical expressions for $\hat{S}(z)$, we observe that the contrast amplitude depends on the coefficients given by R_R , R_0 , and R_1 . In Fig. 4.4 we consider a reflectivity of the reference mirror $R_R = 1$. Figure (4.5) shows how the contrast depends on the R_R in the interferometer. For a reflectivity less than one, the contrast for FD-OCT enhance, while for FD-ICT and FD-SU(1,1) diminish and for quantum FD-OCT remains constant.

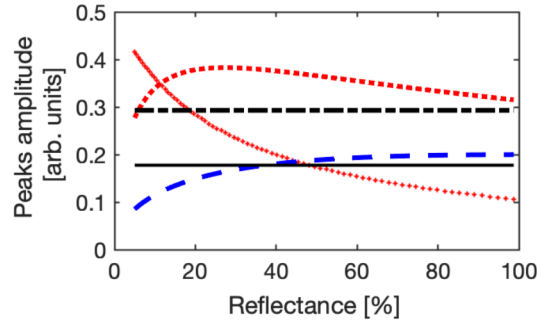


Figure 4.5: The amplitude of the interface contrasts for the reflectance of the reference mirror R_R in the interferometer. Self-interference terms: (+) Standard OCT and (line) QOCT. Cross-correlated interference terms for the first layer R_0 : (dot) Standard OCT, (dot-line) QOCT, (line) SU(1,1) and ICT.

The amplitude of the self-interference peak increase for FD-OCT for a reflectivity less than one, while for FD-QOCT, the amplitude is constant. For cross-interference terms, FD-OCT has a maximum value for a reflectance approx to 20%, while FD-ICT and FD-SU(1,1) the amplitude reduces considerably for a reflectance less than 40%. Therefore, to differentiate the peaks in FD-OCT is more convenient work with a reflectance approx to 20%, while FD-ICT and FD-SU(1,1) a reflectance up to 40% is enough.

4.6 Conclusions

This chapter has developed the theoretical framework to realize optical coherence tomography using nonlinear interferometers working in the Fourier domain. We deduced general expressions for the expected output spectrum and focused our analysis on the particular case of a bi-layer sample. Our formulation allows us to perform a peer comparison, showing the main similarities and differences between the techniques.

All nonlinear techniques allow inferring the optical properties of the sample. We notice that FD-SU(1,1) and FD-ICT are the most error-free methods in identifying the cross-correlation peaks, which carry information about the sample's optical thickness. It is worth mentioning that FD-SU(1,1) has an added advantage: it can work in the high parametric gain, which results in higher photon fluxes and thus lower integration times. Therefore, FD-SU(1,1) might be the closest competitor to the fast acquisitions times found in the classical FD-OCT method.

Deducing the analytical expressions for the spectrograms $\hat{S}(z)$, we explore the dependence of the contrast with respect to the reflectivity of the reference mirror in the interferometer. For a reflectivity less than one, the contrast for FD-OCT enhance, while for FD-ICT and FD-SU(1,1) diminish and for quantum FD-OCT remains constant. These results add valuable information to the growing body of literature concerning applications of nonlinear interferometers.

Chapter 5

Tailoring the axial resolution in induced coherence tomography

Induced coherence tomography is a novel axial-imaging technique with potential applications. It uses the notion of induced coherence between two pairs of down-converted photons to infer the reflectivity profile of a sample, measuring the degree of first-order coherence. The scheme offers the advantage of probing the sample with infrared photons (ideal for biological samples) while using the optimum wavelength for the detection system. In this chapter, we analyze the fundamental factors that define the axial resolution of the method. We found that using ultrashort laser pulses in combination with long nonlinear crystals; the technique achieves micrometer resolutions with a high emission rate of photon pairs. The principal results of this chapter are published in the paper "Frequency-correlation requirements on the biphoton wave function in an induced-coherence experiment between separate sources", *Phys. Rev. A* 102, 053711.

5.1 Introduction

In 1991, Zou *et al.* demonstrated the effect of induced coherence studying the indistinguishability between the signal beams generated by two separate down-converters [28, 109]. Lately, induced coherence shows potential applications in optical imaging. For instance, Barreto *et al.* demonstrate a two-dimensional imaging modality known as imaging with undetected photons, where the probe photons (i.e., the photons interacting with the sample) are not detected [32, 33, 110].

Induced coherence tomography (ICT) appears as an imaging technique resolving the axial profile of a sample [68, 64, 111], akin to optical coherence tomography (see chapter 1). This technique works with two down-converters in a type Mach-Zehnder nonlinear interferometer. In this method, one of the idler modes reflects from a layered sample, which modifies the first-order correlation function between the signal photons, providing information about the sample's internal structure. From a practical point of view, the main advantage of these systems is that one can choose a wavelength for the idler beam that interacts with the sample and is never detected and another wavelength for the signal beam to be detected that enhances photo-detection efficiency. They also can show better sensitivity than alternative schemes

[112, 113].

Previous experiments use continuous wave (CW) pumping in the low parametric gain regime, which produces frequency correlations and frequency entanglement between signal-idler pairs generated in every single source. Here, we study the conditions to achieve the maximum axial resolution of the system. Therefore, we analyze the first-order correlation function between signal modes considering ultrashort pumping. Unexpectedly, we found that the width of the pump pulses limits the resolution, contrary to the CW pumping, where the length of the crystals becomes the limiting factor. Furthermore, the emission rate of photon pairs is independent of the pulse width. These findings imply that we can use femtosecond laser pulses in combination with long-length crystals to increase the axial resolution of the system while having a high emission rate of photon pairs (consequently reducing acquisition times).

5.2 Formalism

Figure 5.1 shows a scheme of an induced coherence experiment with two parametric down-converters (NLC₁ and NLC₂). We consider a pulsed laser that generates coherent light with a spectrum $F(\omega_p)$. The pump's frequency is $\omega_p = \omega_p^0 + \Omega_p$, with ω_p^0 being the central frequency and Ω_p the frequency deviation from the central frequency. A beamsplitter divides the pump beam into two coherent sub-beams that pump the two nonlinear crystals. The two sub-beams travel distances z_{p_1} and z_{p_2} before reaching NLC1 and NLC2, respectively.

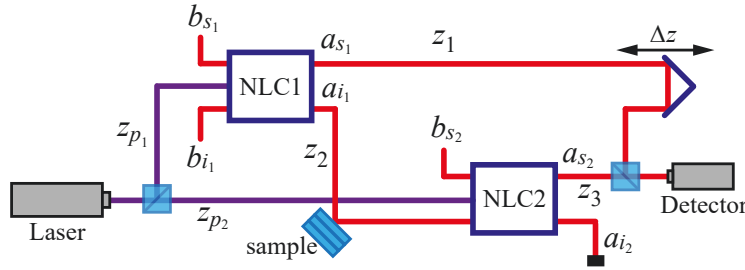


Figure 5.1: Induced coherence between signal photons generated in separate parametric down converters. The idler traverses a lossy sample before being injected into NLC2. The detector measures the interference between signal photons s_1 and s_2 as a function of the path delay Δz . NLC: nonlinear crystal; s, i : signal and idler modes; b, a input and output quantum operators.

Both crystals have nonlinear susceptibility $\chi^{(2)}$ and length L . The nonlinear interaction generates signal and idler photons s_1 and i_1 in NLC1, and s_2 and i_2 in NLC2. The frequency of the signal and idler photons reads $\omega_s = \omega_s^0 + \Omega_s$ and $\omega_i = \omega_i^0 + \Omega_i$, where $\omega_{s,i}^0$ are central frequencies, and $\Omega_{s,i}$ are frequency deviations from the corresponding central frequencies. The conditions $\omega_p^0 = \omega_s^0 + \omega_i^0$ and $\Omega_p = \Omega_s + \Omega_i$ are satisfied.

The quantum operators $a_{s_1, s_2}(\omega_s)$ and $a_{i_1, i_2}(\omega_i)$ correspond to signal and idler modes at the corresponding nonlinear crystals' output face. $b_{s_1, s_2}(\Omega_s)$ and $b_{i_1}(\Omega_i)$ designate the corresponding operators at the input face. In the low parametric gain regime, the Bogoliubov

transformations that relate the input and output operators for NLC1 are [114, 115]:

$$a_{s_1}(\omega_s) = U_s(\omega_s)b_{s_1}(\omega_s) + \int d\omega_i V_{s_1}(\omega_s, \omega_i)b_{i_1}^\dagger(\omega_i), \quad (5.1)$$

$$a_{i_1}(\omega_i) = U_i(\omega_i)b_{i_1}(\omega_i) + \int d\omega_s V_{i_1}(\omega_s, \omega_i)b_{s_1}^\dagger(\omega_s), \quad (5.2)$$

where $U_s(\omega_s) = \exp[ik_s(\omega_s)L]$, $U_i(\omega_i) = \exp[ik_i(\omega_i)L]$ and $V_{s_1, i_1}(\omega_s, \omega_i)$ are the joint signal-idler spectral amplitude given by

$$V_{s_1}(\omega_s, \omega_i) = i(\sigma L)F_{p_1}(\omega_s + \omega_i) \operatorname{sinc} \left[\frac{1}{2} \Delta k(\omega_s, \omega_i) L \right] \times \exp \left[i \frac{k_p(\omega_s + \omega_i) + k_s(\omega_s) - k_i(\omega_i)}{2} L \right], \quad (5.3)$$

$$V_{i_1}(\omega_s, \omega_i) = i(\sigma L)F_{p_1}(\omega_s + \omega_i) \operatorname{sinc} \left[\frac{1}{2} \Delta k(\omega_s, \omega_i) L \right] \times \exp \left[i \frac{k_p(\omega_s + \omega_i) + k_i(\omega_i) - k_s(\omega_s)}{2} L \right]. \quad (5.4)$$

and the nonlinear coefficient σ is [114, 116, 115]

$$\sigma = \left[\frac{\hbar \omega_p^0 \omega_s^0 \omega_i^0 [\chi^{(2)}]^2 N_0}{16\pi \epsilon_0 c^3 n_p n_s n_i A} \right]^{1/2}, \quad (5.5)$$

with N_0 the number of pump photons per pulse, A is the effective area of interaction, and $n_{p,s,i}$ are refractive indexes at the central frequencies of all waves. The pump spectrum F_{p_1} is

$$F_{p_1}(\omega_p) = \frac{T_0^{1/2}}{\pi^{1/4}} \exp \left[-\frac{(\omega_p - \omega_p^0)^2 T_0^2}{2} \right] \exp [ik_p(\omega_p)z_{p_1}], \quad (5.6)$$

here, we have assumed a Gaussian shape for the pump beam spectrum, and T_0 defines the pump pulse's temporal width. The spectral intensity $\propto |F(\omega_p)|^2$ has a $1/e$ full-width of $2/T_0$, suggesting that $F(\omega_p)$ can also describe a cw pump laser if $T_0 \rightarrow \infty$. The signal and idler frequencies are centered at ω_j^0 ($j \equiv s, i$), and hence we can write $\omega_j = \omega_j^0 + \Omega_j$ in terms of the variable $\Omega_j \in (-\infty, \infty)$. The energy condition implies that $\omega_p^0 = \omega_s^0 + \omega_i^0$ and $\Omega_p = \Omega_s + \Omega_i$, where $\Omega_p = \omega_p - \omega_p^0$. These assumptions allow us to apply a first-order Taylor expansion over the wave numbers, i.e., $k_j(\omega_j) = k_j^0 + N_j \omega_j$ ($j \equiv s, i, p$), where N_j are the inverse group velocities. The phase-matching function $\Delta k = k_p(\Omega_s + \Omega_i) - k_s(\Omega_s) - k_i(\Omega_i)$ now reads

$$\Delta k = (N_p - N_s)\Omega_s + (N_p - N_i)\Omega_i, \quad (5.7)$$

where we use the momentum conservation condition $k_p^0 = k_s^0 + k_i^0$.

Referring back to Fig. 5.1, after the NLC1, the idler mode a_{i_1} traverses a distance z_2 before encountering a semi-transparent material composed of N discrete layers. Here, a layer means the interface between two refractive indices. The quantum operator that describes this process is [117, 118]

$$b_{i_2}(\omega_i) \longrightarrow r_i(\omega_i)a_{i_1}(\omega_i) \exp [ik_i(\omega_i)z_2] + f(\omega_i), \quad (5.8)$$

the operator f fulfills the commutation relationship $[f(\Omega), f^\dagger(\Omega')] = (1 - |r_i(\Omega)|^2)\delta(\Omega - \Omega')$ [118]. We model the reflectivity profile as follows:

$$r_i(\omega_i) = \sum_{j=0}^{N-1} r_j e^{-i\omega\tau_j} = r_0 + r_1 e^{-i\omega\tau_1} + r_2 e^{-i\omega\tau_2} + \dots, \quad (5.9)$$

where τ_j is the time traveled in the round-trip from the 0th layer to the j th layer, and r_j is the effective reflection coefficient considering Fresnel coefficients (notice that $r_j \in \mathbb{R}$ by considering normal incidence).

We now consider the SPDC process in the second crystal (NLC2). After the sample interaction, the idler beam is injected into NLC2. In this crystal, the input and output relationship for operators a_{s_2} and a_{i_2} fulfill

$$a_{s_2}(\omega_s) = U_s(\omega_s)b_{s_2}(\omega_s) + \int d\omega_i V_{s_2}(\omega_s, \omega_i)b_{i_2}^\dagger(\omega_i), \quad (5.10)$$

$$a_{i_2}(\omega_i) = U_i(\omega_i)b_{i_2}(\omega_i) + \int d\omega_s V_{i_2}(\omega_s, \omega_i)b_{s_2}^\dagger(\omega_s), \quad (5.11)$$

where V_{s_2, i_2} is analogous to V_{s_1, i_2} in Eq. (5.3) with $F_{p_2} = F_p(\omega_p) \exp[ik_p(\omega_p)z_{p_2}]$.

Calculating the expression of the operator for the photon signal $a_{s_2}(\omega_s)$. From Eq. (5.8)

$$b_{i_2}^\dagger(\omega_i) = r_i^*(\omega_i)a_{i_1}^\dagger(\omega_i) + f^\dagger(\omega_i),$$

and Eq. (5.2)

$$\begin{aligned} a_{i_1}^\dagger(\omega_i) &= b_{i_1}^\dagger(\omega_i) \exp[-ik_i(\omega_i)L - ik_i(\omega_i)z_2] \\ &+ \int d\omega_s V_{i_1}^*(\omega_s, \omega_i)b_{s_1}(\omega_s) \exp[-ik_i(\omega_i)z_2], \end{aligned} \quad (5.12)$$

now

$$\begin{aligned} b_{i_2}^\dagger(\omega_i) &= r_i^*(\omega_i) \left(b_{i_1}^\dagger(\omega_i) \exp[-ik_i(\omega_i)L - ik_i(\omega_i)z_2] \right. \\ &\left. + \int d\omega_s V_{i_1}^*(\omega_s, \omega_i)b_{s_1}(\omega_s) \exp[-ik_i(\omega_i)z_2] \right) + f^\dagger(\omega_i). \end{aligned} \quad (5.13)$$

The signal mode a_{s_2} travels a distance z_3 causing $a_{s_2}(\omega_s) \rightarrow a_{s_2}(\omega_s) \exp(-ik_s(\omega_s)z_3)$. Substituting Eq. (5.13) in Eq. (5.10) the expression for $a_{s_2}(\omega_s)$ is

$$\begin{aligned} a_{s_2}(\omega_s) &= b_{s_2}(\omega_s) \exp[ik_s(\omega_s)L - ik_s(\omega_s)z_3] \\ &+ \int d\omega_i V_{s_2}(\omega_s, \omega_i)r_i^*(\omega_i)b_{i_1}^\dagger(\omega_i) \\ &\exp[-ik_s(\omega_s)z_3 - ik_i(\omega_i)z_2] \\ &+ \int d\omega_i V_{s_2}(\omega_s, \omega_i)r_i^*(\omega_i) \int d\omega_s V_{i_1}^*(\omega_s, \omega_i)b_{s_1}(\omega_s) \\ &\exp[-ik_s(\omega_s)z_3 - ik_i(\omega_i)z_2] \\ &+ \int d\omega_i V_{s_2}(\omega_s, \omega_i)f^\dagger(\omega_i) \exp[-ik_s(\omega_s)z_3]. \end{aligned} \quad (5.14)$$

In the same stage of Fig. 5.1, the signal mode a_{s_1} passes through a controllable delay $\Delta z = cT$ causing $a_{s_1}(\omega_s) \rightarrow a_{s_1}(\omega_s) \exp(-i\omega_s T)$. Then, a 50:50 beamsplitter recombines the signal modes $a_{s_1}(\omega_s)$ and $a_{s_2}(\omega_s)$, and the photodetector measures the single photon counts of the resulting superposition resulting in the interferogram of the sample.

5.2.1 Interferogram

After the beamsplitter, the detector measures the interference between the signal photons s_1 and s_2 . The state of the photon after the beamsplitter is

$$\psi = r_{BS}a_{s_1}(t+T) + t_{BS}a_{s_2}(t)e^{i\frac{\pi}{2}} \quad (5.15)$$

where s_1 has a phase difference given by the delay T . The photodetector records an interferogram of the form

$$\begin{aligned} I(T) &= |r_{BS}|^2 \int dt \langle a_{s_1}^\dagger(t+T)a_{s_1}(t+T) \rangle + |t_{BS}|^2 \int dt \langle a_{s_2}^\dagger(t)a_{s_2}(t) \rangle \\ &\quad + r_{BS}t_{BS}^* e^{i\frac{\pi}{2}} \int dt \langle a_{s_1}^\dagger(t+T)a_{s_2}(t) \rangle \\ &\quad + r_{BS}^* t_{BS} e^{-i\frac{\pi}{2}} \int dt \langle a_{s_2}^\dagger(t)a_{s_1}(t+T) \rangle, \end{aligned} \quad (5.16)$$

for a 50:50 beamsplitter $|r_{BS}|^2 = |t_{BS}|^2 = 1/2$, the normalized probability of detection is

$$I(T) = 1 + \frac{2\sqrt{N_{s_1}N_{s_2}}}{N_{s_1} + N_{s_2}} |g_{s_1,s_2}^{(1)}(T)| \sin(\omega_s^0 T). \quad (5.17)$$

Here, the $|g_{s_1,s_2}^{(1)}(T)|$ is the normalized first-order correlation function, N_{s_1} , and N_{s_2} are the number of signal photons designated as

$$\begin{aligned} N_{s_1} &= \int dt \langle a_{s_1}^\dagger(t)a_{s_1}(t) \rangle, \\ N_{s_2} &= \int dt \langle a_{s_2}^\dagger(t)a_{s_2}(t) \rangle, \end{aligned} \quad (5.18)$$

where we consider that the signal photons are constant i.e. $N_{s_1}(t+T) = N_{s_1}(t)$

5.2.2 The normalized first-order correlation function

The normalized first-order correlation function gives the visibility of the interference fringes detected after combining both signals in a beamsplitter. It is defined through the expected value of the number of photons detected

$$|g_{s_1,s_2}^{(1)}(T)| = \left| \frac{\int dt \langle a_{s_1}^\dagger(t+T)a_{s_2}(t) \rangle}{\sqrt{\int dt \langle a_{s_1}^\dagger(t)a_{s_1}(t) \rangle} \sqrt{\int dt \langle a_{s_2}^\dagger(t)a_{s_2}(t) \rangle}} \right|. \quad (5.19)$$

In order to write the Eq. (5.19) in terms of $a_{s_1}(\omega_s)$ and $a_{s_2}(\omega_s)$, we apply the Fourier transform

$$a_{s_1}(t+T) = \frac{1}{\sqrt{2\pi}} \int d\omega_s a_{s_1}(\omega_s) \exp[-i\omega_s(t+T)],$$

and for the second mode

$$a_{s_2}(t) = \frac{1}{\sqrt{2\pi}} \int d\omega'_s a_{s_2}(\omega'_s) \exp[-i\omega'_s(t)]. \quad (5.20)$$

The correlation

$$\begin{aligned} \int dt \langle a_{s_1}^\dagger(t+T) a_{s_2}(t) \rangle &= \frac{1}{2\pi} \int \int \int dt d\omega_s d\omega'_s \langle a_{s_1}^\dagger(\omega_s) a_{s_2}(\omega'_s) \rangle \\ &\quad \times \exp[i(\omega_s - \omega'_s)t] \exp[i\omega_s T], \end{aligned}$$

using the definition of the Dirac delta function:

$$\delta(x-x') = \frac{1}{2\pi} \int dt \exp[i(x-x')t], \quad (5.21)$$

we get

$$\int dt \langle a_{s_1}^\dagger(t+T) a_{s_2}(t) \rangle = \int \int d\omega_s d\omega'_s \langle a_{s_1}^\dagger(\omega_s) a_{s_2}(\omega'_s) \rangle \delta(\omega_s - \omega'_s) \exp[i\omega_s T]. \quad (5.22)$$

Integrating Eq. (5.22) in ω'_s :

$$\int dt \langle a_{s_1}^\dagger(t+T) a_{s_2}(t) \rangle = \int d\omega_s \langle a_{s_1}^\dagger(\omega_s) a_{s_2}(\omega_s) \rangle \exp[i\omega_s T]. \quad (5.23)$$

The rate of single counts in Eq. 5.18 now reads

$$N_{s_1} = \int d\omega_s \langle a_{s_1}^\dagger(\omega_s) a_{s_1}(\omega_s) \rangle, \quad (5.24)$$

$$N_{s_2} = \int d\omega_s \langle a_{s_2}^\dagger(\omega_s) a_{s_2}(\omega_s) \rangle.$$

The normalized first-order correlation function now reads as

$$|g_{s_1, s_2}^{(1)}(T)| = \frac{|\int d\omega_s \langle a_{s_1}^\dagger(\omega_s) a_{s_2}(\omega_s) \rangle \exp[i\omega_s T]|}{N_{s_1}^{1/2} N_{s_2}^{1/2}}. \quad (5.25)$$

Now, calculating the expected value of the number of photons detected $\langle a_{s_1}^\dagger(\omega_s) a_{s_2}(\omega_s) \rangle$. From Eq. (5.1) together with Eq. (5.14), the correlation is

$$\begin{aligned} \langle a_{s_1}^\dagger(\omega_s) a_{s_2}(\omega_s) \rangle &= \int d\omega_i r_i^*(\omega_i) V_{s_2}(\omega_s, \omega_i) V_{s_1}^*(\omega_s, \omega_i) \\ &\quad \times \exp[ik_s(\omega_s)(z_3 - z_1) - ik_i(\omega_i)z_2], \end{aligned} \quad (5.26)$$

that are the terms that give a non-zero contribution. Writing the integral of Eq. (5.25) as $g^{(1)} = \int d\omega_s \langle a_{s_1}^\dagger(\omega_s) a_{s_2}(\omega_s) \rangle \exp[i\omega_s T]$ and

$$g^{(1)} = \int \int d\omega_s d\omega_i r_i^*(\omega_i) V_{s_2}(\omega_s, \omega_i) V_{s_1}^*(\omega_s, \omega_i) \times \exp[ik_s(\omega_s)(z_3 - z_1) - ik_i(\omega_i)z_2] \exp[i\omega_s T]. \quad (5.27)$$

The signal and idler photon frequencies are centered at ω_j^0 ($j \equiv s, i$), and hence we can write $\omega_j = \omega_j^0 + \Omega_j$ in terms of the variable $\Omega_j \in (-\infty, \infty)$. The wave numbers $k_j(\omega_j) = \omega_j/c$ ($j \equiv s, i, p$) and the optical path $L = n_i L$ added by the second crystal; therefore, $z_2 = n_i L + z_2$. Now we have

$$g^{(1)} = \int \int d\Omega_s d\Omega_i r_i^*(\Omega_i) V_{s_2}(\Omega_s, \Omega_i) V_{s_1}^*(\Omega_s, \Omega_i) \times \exp\left[i\frac{\Omega_s}{c}(z_3 - z_1) - i\frac{\Omega_i}{c}(n_i L + z_2)\right] \exp[i\Omega_s T] \times \exp\left[i\frac{\omega_s^0}{c}(z_3 - z_1) - i\frac{\omega_i^0}{c}(n_i L + z_2)\right] \exp[i\omega_s^0 T], \quad (5.28)$$

with

$$V_{s_2}(\Omega_s, \Omega_i) V_{s_1}^*(\Omega_s, \Omega_i) = (\sigma L)^2 \frac{T_0}{\pi^{1/2}} \exp[-(\Omega_s + \Omega_i)^2 T_0^2] \times \exp\left[i(\Omega_s + \Omega_i) \left(\frac{z_{p2}}{c} - \frac{z_{p1}}{c}\right)\right] \exp\left[i\omega_p^0 \left(\frac{z_{p2}}{c} - \frac{z_{p1}}{c}\right)\right] \times \text{sinc}^2\left[\frac{1}{2}((N_p - N_s)\Omega_s + (N_p - N_i)\Omega_i + \phi_V) L\right], \quad (5.29)$$

and $\phi_V = (N_p - N_s)\omega_s^0 + (N_p - N_i)\omega_i^0$.

To solve for $g_{s_1, s_2}^{(1)}(T)$, it is convenient to define the frequencies $\Omega_\pm = \Omega_s \pm \Omega_i$. This change of variable allows us to write

$$g^{(1)} = \frac{1}{2}(\sigma L)^2 \frac{T_0}{\pi^{1/2}} \exp[i\phi'_0] \times \int \int d\Omega_+ d\Omega_- r_i^*\left(\frac{\Omega_+ - \Omega_-}{2}\right) \exp[-\Omega_+^2 T_0^2 + i\alpha\Omega_+] \times \exp[i\beta\Omega_-] \text{sinc}^2\left[\frac{D_+ L}{2}\Omega_+ + \frac{DL}{4}\Omega_-\right], \quad (5.30)$$

with

$$\alpha = \frac{1}{2} \left(\frac{z_3 - z_1}{c} - \frac{n_i L + z_2}{c} + 2\frac{z_{p2} - z_{p1}}{c} + T \right) \beta = \frac{1}{2} \left(\frac{z_3 - z_1}{c} + \frac{n_i L + z_2}{c} + T \right) \phi'_0 = \frac{\omega_s^0}{c}(z_3 - z_1 + z_{p2} - z_{p1} + cT) - \frac{\omega_i^0}{c}(n_i L + z_2 - z_{p2} + z_{p1}). \quad (5.31)$$

Here, $D = N_i - N_s$ is the group velocity mismatch (GVM) between signal and idler photons, and similarly, $D_+ = N_p - (N_i + N_s)/2$ defines the GVM between the pump photons and the average signal-idler inverse group velocities.

5.3 Results

5.3.1 Axial resolution

Let us consider a single-layer sample described in Eq. (5.9) where $r_i(\omega_i) = r_0$. The first order correlation function in Eq. (5.30) is

$$\begin{aligned}
 g^{(1)} &= 2r_0 \frac{\sigma^2 L}{D} \frac{T_0}{\pi^{1/2}} \exp[i\phi'_0] \\
 &\times \int dx \exp\left[\left(i\beta \frac{4}{DL} x\right)\right] \text{sinc}^2[x] \\
 &\times \int d\Omega_+ \exp\left[-\left(\Omega_+^2 T_0^2 + i\left(\beta \frac{2D_+}{D} - \alpha\right)\Omega_+\right)\right],
 \end{aligned} \tag{5.32}$$

we have made use of the change of variables

$$x = \frac{D_+ L}{2} \Omega_+ + \frac{DL}{4} \Omega_-, \tag{5.33}$$

$$\Omega_- = \frac{4}{DL} \left(x - \frac{D_+ L}{2} \Omega_+\right), \tag{5.34}$$

$$d\Omega_- = \frac{4}{DL} dx. \tag{5.35}$$

Solving the integrals and rewriting the correlation function in Eq. (5.32)

$$\begin{aligned}
 g^{(1)} &= 2\pi r_0 \frac{\sigma^2 L}{D} \exp[i\phi'_0] \\
 &\times \exp\left[-\frac{\left(\left[1 - \frac{2D_+}{D}\right] T_1 + 2T_2\right)^2}{16T_0^2}\right] \text{tri}\left(\frac{T_1}{DL}\right),
 \end{aligned} \tag{5.36}$$

where

$$\begin{aligned}
 T_1 &= \frac{z_3 + n_i L + z_2 - z_1}{c} + T, \\
 T_2 &= \frac{z_{p2} - z_{p1} - n_i L - z_2}{c}.
 \end{aligned} \tag{5.37}$$

The number of signal photons generated per pulse designated in Eq. (5.24) is

$$N_{s_1} = N_{s_2} = \int \int d\Omega_s d\Omega_i |V(\Omega_s, \Omega_i)|^2 = 2\pi \frac{\sigma^2 L}{D}. \tag{5.38}$$

Notice that the photon flux is independent of the shape of the pulse.

To optimize the pulsed parametric amplification in NLC2, one needs to synchronize the pump and idler pulses' arrival time to the nonlinear crystal [67]. Therefore, the condition $z_{p2} = z_{p1} + cN_i L + z_2$ must be fulfilled, so that $T_2 = 0$. Using Eq. (5.36) and (5.38) into Eq. (5.32), the normalized first-order correlation function can be written as

$$\left|g_{s_1, s_2}^{(1)}(T_1, T_2)\right| = \text{tri}\left(\frac{T_1}{DL}\right) \exp\left[-\frac{1}{16T_0^2} \left[\left(1 - \frac{2D_+}{D}\right) T_1 + 2T_2\right]^2\right]. \tag{5.39}$$

Therefore, the first-order correlation function is the product of a triangular function of width DL and a Gaussian function of width T_0 . Figure 5.2 plots the triangular and Gaussian functions in Eq. (5.39) as a function of $\Delta z = z_3 - z_1 + z_2 + cN_iL$. We consider two MgO-doped lithium niobate crystals ($\chi^{(2)} = 28$ pm/V) pumped by a pulsed laser operating at $\lambda_p^0 = 532$ nm of pulses with temporal widths of $T_0 = 100, 2$ and 0.1 ps. The resulting signal and idler photons have wavelengths $\lambda_s^0 = 810$ nm and $\lambda_i^0 = 1550$ nm with $D_- = -263.50$ fs/mm and $D_+ = 780$ fs/mm. The first row of Fig. 5.2 shows the results for $L = 5$ mm, and the second row for $L = 10$ mm.

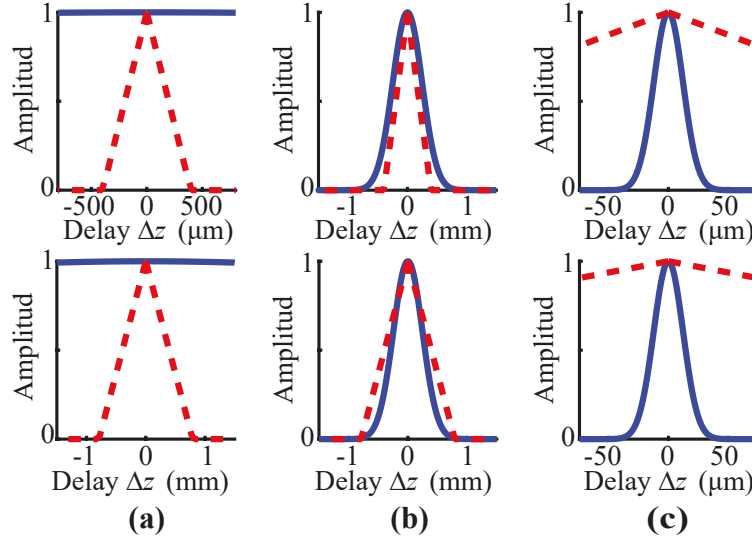


Figure 5.2: Triangular (red dotted line) and Gaussian (solid blue line) functions describing the degree of first-order coherence $g_{s1,s2}^{(1)}$ [Eq. (5.39)]. We consider nonlinear crystals with lengths $L = 5$ mm (first row) and $L = 10$ mm (second row) and a pumping pulsed laser of (a) $T_0 = 100$ ps, (b) $T_0 = 2$ ps, and (c) $T_0 = 100$ fs.

The simulations demonstrate how the temporal width T_0 redefines the width of $g_{s1,s2}^{(1)}$. For picosecond pulses ($T_0 = 100$ ps and 2 ps), the triangular function defines the spatial resolution, which has a coherence length given by $l_T = cDL$. In contrast, for ultrashort pulses and millimeter-length crystals, the coherence length is $l_G = 8(\ln 2)^{1/2}(1 - 2(D_+/D))^{-1}cT_0$, which corresponds to the full width at half maximum (FWHM) of the Gaussian function.

5.3.2 Coherent length and bandwidth

For further illustration of the spatial resolution given by Eq. (5.39), Fig. 5.3(a) shows the total coherence length l_c as the FWHM for both cases ($L = 5$ mm and 10 mm) in terms of T_0 ranging from the femtosecond to the picosecond domain. Figure. 5.3(b) shows the bandwidth of the signal-photon spectrum $P_s(\omega_s)$ given by

$$P(\Omega_s) = \int d\Omega_p |V_{s1}(\Omega_s, \Omega_i)|^2, \quad (5.40)$$

from Eq. (5.29)

$$P(\Omega_s) = (\sigma L)^2 \frac{T_0}{\sqrt{\pi}} \int d\Omega_p \exp[-\Omega_p T_0^2] \operatorname{sinc}^2\left(\frac{D_1 \Omega_p L}{2} + \frac{D \Omega_s L}{2}\right), \quad (5.41)$$

where $D_1 = N_p - N_i$. Here, the nonlinear coefficient of Eq. (5.5) is $\sigma = 2.62 \times 10^{-5} \text{ s}^{1/2} \text{ m}^{-1}$, considering $n_p^0 = 2.26$, $n_s^0 = 2.20$, $n_i^0 = 2.16$ [119], the pump beam has a pulse energy of 4 nJ [120], and illuminates an area of 0.10 mm^2 .

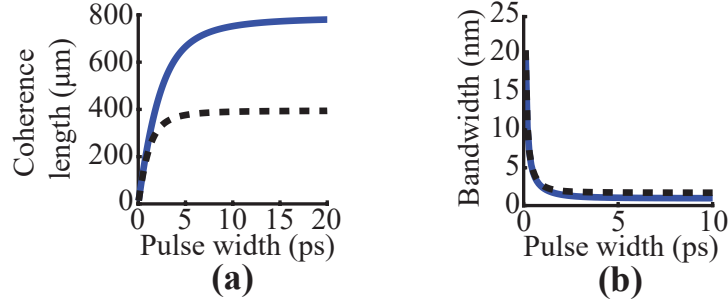


Figure 5.3: (a) Coherence length in terms of the pulse width T_0 . (b) The bandwidth of the signal-photon spectrum. We consider nonlinear crystals with lengths $L = 5 \text{ mm}$ (black dotted lines) and $L = 10 \text{ mm}$ (blue solid lines).

According to our simulations in Fig. 5.3, it seems feasible to achieve a micrometer resolution using ultrashort pulses and millimeter-length nonlinear crystals. Such resolution is comparable with current commercially available OCT systems [121]. The number of down-converted signal photons generated per pulse N_{s_1, s_2} is given by Eq. (5.38), where the pulse duration T_0 does not contribute to the number of signal photons generated. Hence, Eqs. (5.38) and (5.39) imply that we can increase the rate of the signal photon (by increasing L) while maintaining a high spatial resolution (by decreasing T_0).

5.3.3 Time domain induce coherence tomography of a bi-layer sample

The first-order correlation function is the measure of axial resolution in an OCT system. The Equation (5.39) shows that one can obtain a narrow first-order correlation function and high axial resolution, even for a long nonlinear crystal, using an ultrashort pump pulse. To show this effect, we consider a bi-layer sample characterized by reflectivity

$$r_i(\Omega) = r_0 + r_1 \exp[i(\omega_i^0 + \Omega_i)\tau] \quad (5.42)$$

with $\tau = 2d_0 n_0 / c$ the delay where d_0 and n_0 designate the thickness and refractive index, respectively, of the sample. The coefficient r_0 is the Fresnel coefficient for the first layer, whereas r_1 is the effective coefficient for the second layer, taking into account propagation through the sample. z_2 is the distance traveled by the idler beam reflected from the first layer, while $z_2 + 2n_0 d_0$ is the optical distance traveled by the idler beam reflected from the second layer.

Substituting Eq. (5.42) in Eq. (5.28), the first-order correlation for a bi-layer sample is

$$\begin{aligned}
 \int d\Omega_s \langle a_{s1}^\dagger(\Omega_s) a_{s2}(\Omega_s) \rangle \exp[i\Omega_s T] &= r_0^* \int \int d\Omega_s d\Omega_i \\
 &\times V_{p2}(\Omega_s, \Omega_i) V_{p1}^*(\Omega_s, \Omega_i) \\
 &\times \exp \left[i \frac{\Omega_s}{c} (z_3 - z_1) - i \frac{\Omega_i}{c} (n_i L + z_2) \right] \exp^{i\Omega_s T} \\
 &\times \exp \left[i \frac{\omega_s^0}{c} (z_3 - z_1) - i \frac{\omega_i^0}{c} (n_i L + z_2) \right] \exp^{i\omega_s^0 T} \\
 &+ r_1^* \exp(i\omega_i^0 \tau) \int \int d\Omega_s d\Omega_i (\exp(i\Omega_i \tau) \\
 &\times V_{p2}(\Omega_s, \Omega_i) V_{p1}^*(\Omega_s, \Omega_i) \\
 &\times \exp \left[i \frac{\Omega_s}{c} (z_3 - z_1) - i \frac{\Omega_i}{c} (n_i L + z_2) \right] \exp^{i\Omega_s T} \\
 &\times \exp \left[i \frac{\omega_s^0}{c} (z_3 - z_1) - i \frac{\omega_i^0}{c} (n_i L + z_2) \right] \exp^{i\omega_s^0 T}
 \end{aligned} \tag{5.43}$$

The first term gives the first layer's information and can be written as Eq. (5.32). The second term is associated with the second layer. Rewriting the second term and using $\Omega_\pm = \Omega_s \pm \Omega_i$, this change of variable allows us to write

$$\begin{aligned}
 \text{second layer} &= \frac{1}{2} r_1 \int \int d\Omega_+ d\Omega_- V_{p2}(\Omega_+, \Omega_-) V_{p1}^*(\Omega_+, \Omega_-) \\
 &\times \exp \left[i \frac{\Omega_+}{2} \frac{z_3 - z_1}{c} - i \frac{\Omega_+}{2} \frac{n_i L + z_2 - 2nd}{c} + i \frac{\Omega_+}{2} T \right] \\
 &\times \exp \left[i \frac{\Omega_-}{2} \frac{z_3 - z_1}{c} + i \frac{\Omega_-}{2} \frac{n_i L + z_2 - 2nd}{c} + i \frac{\Omega_-}{2} T \right] \\
 &\times \exp \left[i \frac{\omega_s^0}{c} (z_3 - z_1) - i \frac{\omega_i^0}{c} (n_i L + z_2 - 2nd) \right] \exp^{i\omega_s^0 T},
 \end{aligned} \tag{5.44}$$

Substituting Eqs. (5.29) in (5.44)

$$\begin{aligned}
 \text{second layer} &= \frac{1}{2} (\sigma L)^2 \frac{T_0}{\pi^{1/2}} \exp[i\phi_0''] r_1 \\
 &\times \int \int d\Omega_+ d\Omega_- \exp[-\Omega_+^2 T_0^2 + i\alpha' \Omega_+] \\
 &\times \exp[i\beta' \Omega_-] \text{sinc}^2 \left[\frac{D_+ L}{2} \Omega_+ + \frac{DL}{4} \Omega_- \right]
 \end{aligned} \tag{5.45}$$

where

$$\begin{aligned}
 \alpha' &= \frac{1}{2} \left(\frac{z_3 - z_1}{c} - \frac{n_i L + z_2}{c} + 2 \frac{z_{p2} - z_{p1}}{c} + (T + \tau) \right) \\
 \beta' &= \frac{1}{2} \left(\frac{z_3 - z_1}{c} + \frac{n_i L + z_2}{c} + (T - \tau) \right) \\
 \phi_0'' &= \frac{\omega_s^0}{c} (z_3 - z_1 + z_{p2} - z_{p1} + cT) - \frac{\omega_i^0}{c} (n_i L + z_2 - z_{p2} + z_{p1} - 2nd)
 \end{aligned} \tag{5.46}$$

Solving the Eq. (5.45) analogous to Eq. (5.32), we have

$$\begin{aligned} \text{second layer} &= 2\pi r_1 \frac{\sigma^2 L}{D} \exp[i\phi_0''] \\ &\times \exp\left[-\frac{\left(\left(1 - \frac{2D_+}{D}\right)T_1 + \left(1 + \frac{2D_+}{D}\right)\tau + 2T_2\right)^2}{16T_0^2}\right] \text{tri}\left(\frac{T_1 - \tau}{DL}\right) \end{aligned} \quad (5.47)$$

Substituting the Eq. (5.43) and (5.38) in Eq. (5.25), the normalized first-order correlation for the bi-layer sample is

$$\begin{aligned} |g_{s_1, s_2}^{(1)}(T)| &= \exp[i\phi_0'] \left[r_0 \exp\left[-\frac{\left(\left(1 - \frac{2D_+}{D}\right)T_1 + 2T_2\right)^2}{16T_0^2}\right] \text{tri}\left(\frac{T_1}{DL}\right) \right. \\ &\quad \left. + r_1 \exp(i\omega_i^0 \tau) \exp\left[-\frac{\left(\left(1 - \frac{2D_+}{D}\right)T_1' + 2T_2'\right)^2}{16T_0^2}\right] \text{tri}\left(\frac{T_1'}{DL}\right) \right] \end{aligned} \quad (5.48)$$

where $T_1' = T_1 - \tau$ and $T_2' = T_2 + \tau$. T_1 and T_2 are given by Eq. (5.37).

The interference signal in Eq. (5.17) at one output port of the beamsplitter is

$$\begin{aligned} N &= N_{s_1} \left\{ 1 + r_0 g_{s_1, s_2}^{(1)}(T_1, T_2) \sin\left[\phi_0 - \frac{\omega_s^0}{c}(z_1 - z_3)\right] \right. \\ &\quad \left. + r_1 g_{s_1, s_2}^{(1)}(T_1', T_2') \sin\left[\phi_0 - \frac{\omega_i^0}{c}2n_0d_0 - \frac{\omega_s^0}{c}(z_1 - z_3)\right], \right. \end{aligned} \quad (5.49)$$

with $\phi_0 = (\omega_p^0/c)(z_{p_2} - z_{p_1}) - (\omega_i^0/c)(z_2 + n_i L)$. We can choose $z_{p_2} = z_{p_1} + cN_i L + z_2$.

The Figure 5.4 shows the photon flux N as a function of Δz for a 20 μm glass slab (refractive index $n_0 = 1.5$) embedded between air ($n_1 = 1$) and water ($n_2 = 1.3$). We consider three scenarios. Figure 5.4(a) considers a pump beam with $T_0 = 100$ ps (quasi-cw) and a crystal with $L = 0.5$ mm. The interferogram shows two maxima separated by 60 μm , the sample's optical path length $c\tau$. Figure 5.4(b) considers the same pulse duration, but $L = 10$ mm. The interferogram cannot resolve the thickness of the sample; there is not enough axial resolution. Figure 5.4(c) considers the same length $L = 10$ mm but now with $T_0 = 100$ fs.

The interferogram recovers the two maxima, thereby resolving the layers of the sample. The two maxima are separated by 42 μm , which is smaller than the sample's optical thickness. This result can be understood noticing that the peak of the interferogram when the shape of the first-order correlation function is dominated by the Gaussian function will take place for a value of T_1 [see Eq. (5.39)],

$$\begin{aligned} \left(1 - \frac{2D_+}{D}\right)(T_1 + \tau) - 2\tau &= 0, \\ \implies T_1 &= \frac{D + 2D_+}{D - 2D_+}\tau. \end{aligned} \quad (5.50)$$

Taking into account the values of $D = -263$ fs/mm and $D_+ = 780$ fs/mm, the factor $(D + 2D_+)/(D - 2D_+) = -0.71$. The separation between the two maxima corresponding to

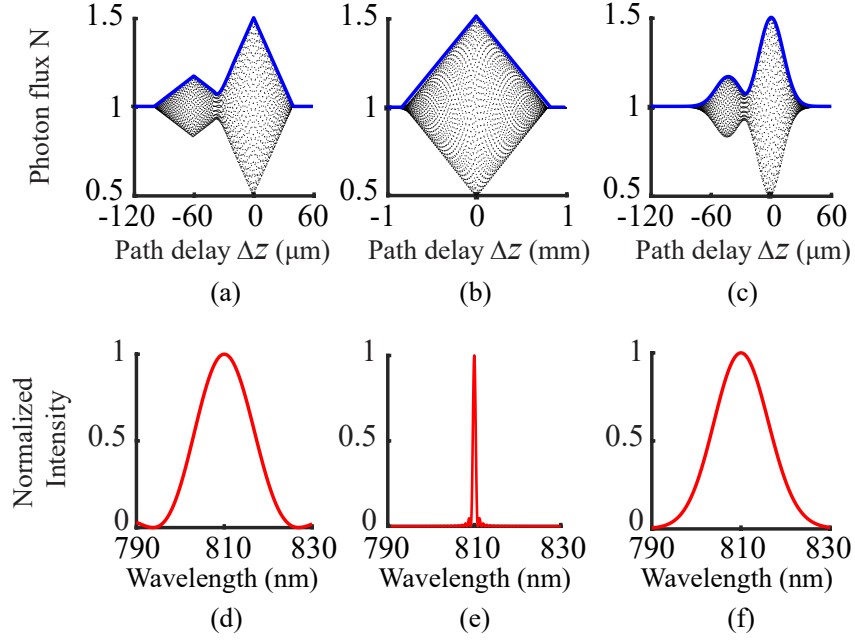


Figure 5.4: Signal N in one output port of the beamsplitter as a function of Δz for a bi-layer sample (first row). We assume a 20 μm glass slab with a refractive index $n = 1.5$ embedded between air and water. We consider three different combinations for the length L of the nonlinear crystals and pump pulses duration T_0 . (a) $L = 0.5$ mm, $T_0 = 100$ ps, (b) $L = 10$ mm, $T_0 = 100$ ps, and (c) $L = 10$ mm, $T_0 = 100$ fs. For illustrative purposes, we consider fringes oscillating with a wavelength larger than the actual signal-photon wavelength of 810 nm. The second row shows the normalized spectrum of the signal photon of bandwidths (d) 14.8 nm, (e) 0.8 nm and (f) 20 nm.

the two layers is $-0.71 \times 60 \mu\text{m} \sim -42 \mu\text{m}$. This result is reminiscent of the fact that after reflection from the sample, we have two pulses separated by τ that are injected in the second nonlinear crystal, and both show a certain delay with the pump pulse [122]. For a case with $D_+ = 0$, we would again have $T_1 = \tau$ as in the quasi-cw case.

Figure 5.4 also shows the signal spectrum given by eq. (5.41). The interferograms and spectra show the reciprocal relation between the spectral bandwidth and axial resolution.

5.4 Conclusions

We have presented a theoretical study of induced coherence tomography considering pulsed pumping. We have found the expressions for the degree of first-order coherence between signal photons considering single-layer and bi-layer samples. In these expressions, Eqs. (5.39) and (5.49), it is now clear the role of the pump pulses in defining the spatial resolution of the system. We also derived simple expressions for the emission rate of signal photons.

For ultrashort pump pulses, the emission rate of signal photons turns out to be linearly dependent on the length of the crystal, regardless of the duration of the pump pulses. Therefore, induced coherence tomography can now benefit from high spatial resolutions and high

emission rates by combining ultrashort pumping with millimeter-length crystals, while maintaining its salutary features, i.e., probing the sample with high resolution at the ideal wavelength, and using the optimum wavelength for detection.

In the low parametric gain regime, photon pairs' emission rate increases with the length of the nonlinear crystal, regardless of the pump pulse duration. We have shown that an OCT scheme based on induced coherence can achieve high axial resolution and high photon-emission rates by combining ultrashort pumping with long crystals. The method maintains its salutary features, i.e., probing the sample with photons centered at the most appropriate wavelength while using the optimum wavelength for photodetectors.

Chapter 6

Conclusions and future work

6.1 Conclusions

In this thesis work, we study optical depth sectioning techniques based on quantum principles. We provide advances in the development of detection methods, analysis of detection schemes, and improved image resolution performance.

Our methodology for photon counting and timing using an oscilloscope allows developing quantum optics experiments, overcoming the limitation of using specialized and relatively expensive equipment. This is advantageous because the oscilloscope is widely used and standard laboratory equipment in STEM laboratories; therefore, its manipulation could be easy.

The methodology was tested by measuring the photon coincidences demonstrating the difference between an entangled and non-entangled photon source. This methodology complements the efforts to generate accessible and low-cost experimental arrangements to potentiate the experimental study of quantum optics. We observe great opportunity of application in undergraduate students' practices as evidenced by our research "Understanding the basic concepts and tools in experimental quantum optics," Proc. SPIE 10741, Optics Education and Outreach V, 107410T (14 September 2018).

Our study of the experimental optical sectioning techniques inspired by OCT provides the theoretical elements to simulate the acquisition of images of the SU (1,1), ICT, and QOCT techniques operated in the Fourier domain. From an experimental perspective, working in this regime allows faster image acquisition, a critical condition for medical applications.

We developed the analysis of a bi-layer sample used as a reference in current experimental studies. The differences between the detection schemes make it difficult to carry out an experimental comparative study of the techniques. With the deduction of the mathematical expressions presented, we can generate simulations of image acquisitions that can serve as references to create training exercises to interpret images of more complex samples. A valuable point is the notation and diagrams used since they allow an easy analysis in the fundamentals of interferometry and the practical part of image interpretation. Based on the simulations, we can argue that the SU (1,1) and ICT schemes provide images where it is easier to interpret the distinction of the layers in a sample.

On the other hand, the advantage of QOCT is a resolution twice better than SU (1,1) and ICT. However, the images taken by QOCT have an effect interpreted as an extra layer that represents a risk in interpreting the image. This effect is generated by the phase of the

pumping beam on the photons interference pattern. Nevertheless can be removed.

It is essential to mention that in the Fourier domain, the position of the sample is crucial. The sample position defines the points that denote the beginning and end of a layer in the spectrogram. Therefore, to avoid overlap and, consequently, erroneous testing of the sample, the distance of the sample must be greater than twice its optical thickness to the point where the optical paths of the signal and idler photons are equal.

As a result of comparing the classical and quantum methods, we conclude that taking advantage of induced coherence and the two photons interference known as the Hong-Ou-Mandel effect potentiate quantum imaging techniques as promising developments on quantum technologies.

For our study of Time domain-ICT, we deduce the operating conditions to overcome the limit of axial resolution given by the length of the non-linear crystal used in the sources of entangled photon pairs that comprise it. We demonstrate that the system coherence length depends on the pumping pulse duration and the crystal length. Our results suggest that using femtosecond pulses combined with long crystals (of the order of mm) is possible to obtain submicrometric resolutions and high fluxes of entangled photons. Therefore, we get an optimized technique for the acquisition of high-resolution images with low acquisition times. According to our research, we find it feasible and exciting to demonstrate these results experimentally.

Finally, based on the previous arguments, we conclude that the present research work provides experimental, theoretical, and modeling elements for the advancement of quantum imaging.

6.2 Future work

It is interesting to know the axial resolution limit to distinguish two layers of an image acquired by the exposed methods. Recent works apply the Fisher information formalism to study the superresolutions. These studies have been used in studies to super the diffraction limit and distinguish two punctual light sources [123, 124, 125, 126]. Therefore, as future work, I propose applying the Fisher information formalism to the techniques presented to study multilayer samples with submicrometric thicknesses.

Along the same lines, the work of Cascade-OCT was presented recently. Here, the FD-OCT arrangement is modified by adding an interferometer that automatically performs the Fourier transform of the spectrogram substituting the computational processing to obtain the Fourier transform to interpret the spectrogram of the sample in analysis [127]. As future work, this arrangement of cascade interferometers could be applied within the SU (1,1), ICT and QOCT systems to investigate their performance.

Another immediate proposal is to develop the FD-ICT analysis considering a pulsed pumping beam like the one carried out in chapter 5. Suppose we hypothesize that the advantages obtained in the time domain are maintained, i.e., submicrometric resolutions and high photon fluxes, and combined with the fast detection speed of the Fourier domain, then the technique would be highly optimized.

Bibliography

- [1] José-Angel Conchello and Jeff W Lichtman. Optical sectioning microscopy. *Nature methods*, 2(12):920–931, 2005.
- [2] Wolfgang Drexler and James G Fujimoto. *Optical coherence tomography: technology and applications*. Springer Science & Business Media, 2008.
- [3] Optical Coherent Tomography News. <http://www.octnews.org/>.
- [4] Silke Aumann, Sabine Donner, Jörg Fischer, and Frank Müller. *Optical Coherence Tomography (OCT): Principle and Technical Realization*, pages 59–85. Springer International Publishing, Cham, 2019.
- [5] Michelle L Gabriele, Gadi Wollstein, Hiroshi Ishikawa, Juan Xu, Jongsick Kim, Larry Kagemann, Lindsey S Folio, and Joel S Schuman. Three dimensional optical coherence tomography imaging: advantages and advances. *Progress in retinal and eye research*, 29(6):556–579, 2010.
- [6] Mehreen Adhi and Jay S Duker. Optical coherence tomography—current and future applications. *Current opinion in ophthalmology*, 24(3):213, 2013.
- [7] Josef F Bille. High resolution imaging in microscopy and ophthalmology: new frontiers in biomedical optics. 2019.
- [8] Michalina J Gora, Melissa J Suter, Guillermo J Tearney, and Xingde Li. Endoscopic optical coherence tomography: technologies and clinical applications. *Biomedical optics express*, 8(5):2405–2444, 2017.
- [9] Jonas Olsen, Jon Holmes, and Gregor BE Jemec. Advances in optical coherence tomography in dermatology—a review. *Journal of biomedical optics*, 23(4):040901, 2018.
- [10] Tianshi Wang, Wolfgang Wieser, Geert Springeling, Robert Beurskens, Charles T Lancee, Tom Pfeiffer, Antonius FW van der Steen, Robert Huber, and Gijs van Soest. Intravascular optical coherence tomography imaging at 3200 frames per second. *Optics letters*, 38(10):1715–1717, 2013.
- [11] Mobin Ibne Mokbul. Optical coherence tomography: basic concepts and applications in neuroscience research. *Journal of medical engineering*, 2017, 2017.
- [12] James Fujimoto and David Huang. Foreword: 25 years of optical coherence tomography. *Investigative ophthalmology & visual science*, 57(9):OCTi–OCTii, 2016.

- [13] James Fujimoto and Eric Swanson. The development, commercialization, and impact of optical coherence tomography. *Investigative ophthalmology & visual science*, 57(9):OCT1–OCT13, 2016.
- [14] Eric A Swanson and James G Fujimoto. The ecosystem that powered the translation of oct from fundamental research to clinical and commercial impact. *Biomedical optics express*, 8(3):1638–1664, 2017.
- [15] David Huang, Eric A Swanson, Charles P Lin, Joel S Schuman, William G Stinson, Warren Chang, Michael R Hee, Thomas Flotte, Kenton Gregory, Carmen A Puliafito, et al. Optical coherence tomography. *science*, 254(5035):1178–1181, 1991.
- [16] Adolph F Fercher, Ch K Hitzenberger, G Kamp, and Sy Y El-Zaiat. Measurement of intraocular distances by backscattering spectral interferometry. *Optics communications*, 117(1-2):43–48, 1995.
- [17] R Leitgeb, CK Hitzenberger, and Adolf F Fercher. Performance of fourier domain vs. time domain optical coherence tomography. *Optics express*, 11(8):889–894, 2003.
- [18] Chang-Wei Sun, Su-Heng Wu, Jia-Chen Duan, Jian-Wei Zhou, Jun-Lei Xia, Ping Xu, Zhenda Xie, Yan-Xiao Gong, and Shi-Ning Zhu. Compact polarization-entangled photon-pair source based on a dual-periodically-poled ti: Linbo 3 waveguide. *Optics letters*, 44(22):5598–5601, 2019.
- [19] Jin Liu, Rongbin Su, Yuming Wei, Beimeng Yao, Saimon Filipe Covre da Silva, Ying Yu, Jake Iles-Smith, Kartik Srinivasan, Armando Rastelli, Juntao Li, et al. A solid-state source of strongly entangled photon pairs with high brightness and indistinguishability. *Nature nanotechnology*, 14(6):586–593, 2019.
- [20] Ayman F Abouraddy, Bahaa EA Saleh, Alexander V Sergienko, and Malvin C Teich. Entangled-photon fourier optics. *JOSA B*, 19(5):1174–1184, 2002.
- [21] Daniel S Tasca, Matthew P Edgar, Frauke Izdebski, Gerald S Buller, and Miles J Padgett. Optimizing the use of detector arrays for measuring intensity correlations of photon pairs. *Physical Review A*, 88(1):013816, 2013.
- [22] Hugo Defienne, Matthew Reichert, and Jason W Fleischer. General model of photon-pair detection with an image sensor. *Physical review letters*, 120(20):203604, 2018.
- [23] Xiaoyu Zhang, Yifan Chen, Kefu Ning, Can Zhou, Yutong Han, Hui Gong, and Jing Yuan. Deep learning optical-sectioning method. *Optics express*, 26(23):30762–30772, 2018.
- [24] Mark Christopher, Akram Belghith, Robert N Weinreb, Christopher Bowd, Michael H Goldbaum, Luke J Saunders, Felipe A Medeiros, and Linda M Zangwill. Retinal nerve fiber layer features identified by unsupervised machine learning on optical coherence tomography scans predict glaucoma progression. *Investigative ophthalmology & visual science*, 59(7):2748–2756, 2018.

- [25] Tariq Mehmood Aslam, David Charles Hoyle, Vikram Puri, and Goncalo Bento. Differentiation of diabetic status using statistical and machine learning techniques on optical coherence tomography angiography images. *Translational vision science & technology*, 9(4):2–2, 2020.
- [26] ZY Ou, CK Hong, and L Mandel. Relation between input and output states for a beam splitter. *Optics communications*, 63(2):118–122, 1987.
- [27] Frédéric Bouchard, Alicia Sit, Yingwen Zhang, Robert Fickler, Filippo M Miatto, Yuan Yao, Fabio Sciarrino, and Ebrahim Karimi. Two photon interference: The hong-ou-mandel effect. *Reports on Progress in Physics*, 2020.
- [28] XY Zou, Lei J Wang, and Leonard Mandel. Induced coherence and indistinguishability in optical interference. *Physical review letters*, 67(3):318, 1991.
- [29] Ayman F Abouraddy, Magued B Nasr, Bahaa EA Saleh, Alexander V Sergienko, and Malvin C Teich. Quantum-optical coherence tomography with dispersion cancellation. *Physical Review A*, 65(5):053817, 2002.
- [30] Magued B Nasr, Bahaa EA Saleh, Alexander V Sergienko, and Malvin C Teich. Demonstration of dispersion-canceled quantum-optical coherence tomography. *Physical review letters*, 91(8):083601, 2003.
- [31] Masayuki Okano, Hwan Hong Lim, Ryo Okamoto, Norihiko Nishizawa, Sunao Kurimura, and Shigeki Takeuchi. $0.54 \mu\text{m}$ resolution two-photon interference with dispersion cancellation for quantum optical coherence tomography. *Scientific reports*, 5(1):1–8, 2015.
- [32] Gabriela Barreto Lemos, Victoria Borish, Garrett D Cole, Sven Ramelow, Radek Lapkiewicz, and Anton Zeilinger. Quantum imaging with undetected photons. *Nature*, 512(7515):409–412, 2014.
- [33] Mayukh Lahiri, Radek Lapkiewicz, Gabriela Barreto Lemos, and Anton Zeilinger. Theory of quantum imaging with undetected photons. *Physical Review A*, 92(1):013832, 2015.
- [34] Marta Gilaberte Basset, Frank Setzpfandt, Fabian Steinlechner, Erik Beckert, Thomas Pertsch, and Markus Gräfe. Perspectives for applications of quantum imaging. *Laser & Photonics Reviews*, 13(10):1900097, 2019.
- [35] Tianshi Wang, Tom Pfeiffer, Evelyn Regar, Wolfgang Wieser, Heleen van Beusekom, Charles T Lancee, Geert Springeling, Ilona Krabbendam, Antonius FW van der Steen, Robert Huber, et al. Heartbeat oct: in vivo intravascular megahertz-optical coherence tomography. *Biomedical optics express*, 6(12):5021–5032, 2015.
- [36] Erika Vallejo Mesa, Héctor Fernando Gómez Goyeneche, and Luz Catherine Martínez Malo. Angiografía por tomografía de coherencia óptica: una nueva herramienta diagnóstica. *Revista Sociedad Colombiana de Oftalmología*, 51(1):63–71, 2018.

- [37] Marco A Aguilar-Pérez, Oscar Fernández-Vizcaya, Elisa D Alegría-Gómez, Regina Velasco-Ramos, Oscar Baca-Lozada, Héctor J Pérez-Cano, Elsa Saldaña-Rivera, and Cristina Pacheco-del Valle. Patrones morfológicos corneales, detectados por medio de tomografía de coherencia óptica de dominio espectral, en pacientes con queratitis infecciosa. *Revista Mexicana de Oftalmología*, 93(2):63–68, 2019.
- [38] Elizabeth Arzuaga Hernández, Maikel Batista Peña, Daylin Cárdenas Chacón, Liset Sánchez Acosta, and Dayamis Núñez Fuentes. Utilidad de la tomografía de coherencia óptica macular en pacientes con glaucoma y alta miopía. *Revista Cubana de Oftalmología*, 33(4), 2020.
- [39] A.F. Fercher, C.K. Hitzenberger, G. Kamp, and S.Y. El-Zaiat. Measurement of intraocular distances by backscattering spectral interferometry. *Optics Communications*, 117(1):43 – 48, 1995.
- [40] Graham R Goldberg, Pavlo Ivanov, Nobuhiko Ozaki, David TD Childs, Kristian M Groom, Kenneth L Kennedy, and Richard A Hogg. Gallium nitride light sources for optical coherence tomography. In *Gallium Nitride Materials and Devices XII*, volume 10104, page 101041X. International Society for Optics and Photonics, 2017.
- [41] Xiao Shu, Lisa Jane Beckmann, and Hao F Zhang. Visible-light optical coherence tomography: a review. *Journal of biomedical optics*, 22(12):121707, 2017.
- [42] Niels M Israelsen, Christian R Petersen, Ajanta Barh, Deepak Jain, Mikkel Jensen, Günther Hanneschläger, Peter Tidemand-Lichtenberg, Christian Pedersen, Adrian Podoleanu, and Ole Bang. Real-time high-resolution mid-infrared optical coherence tomography. *Light: Science & Applications*, 8(1):1–13, 2019.
- [43] Ceyhun Akcay, Pascale Parrein, and Jannick P Rolland. Estimation of longitudinal resolution in optical coherence imaging. *Applied optics*, 41(25):5256–5262, 2002.
- [44] Eugene Hecht. *Optics*. Pearson Education, 2017.
- [45] Machado. G. J., Frascella. G., J. P. Torres, and M. V. Chekhova. Optical coherence tomography with a nonlinear interferometer in the high parametric gain regime. *App. Phys. Letters*, 117:094002, 2020.
- [46] Matthew D Eisaman, Jingyun Fan, Alan Migdall, and Sergey V Polyakov. Invited review article: Single-photon sources and detectors. *Review of scientific instruments*, 82(7):071101, 2011.
- [47] M. V. Chekhova and Z. Y. Ou. Nonlinear interferometers in quantum optics. *Adv. Opt. Photonics*, 8(1):104–155, 2016.
- [48] Zhe-Yu Jeff Ou. *Multi-photon quantum interference*, volume 43. Springer, 2007.
- [49] Christophe Couteau. Spontaneous parametric down-conversion. *Contemporary Physics*, 59(3):291–304, 2018.

- [50] David C Burnham and Donald L Weinberg. Observation of simultaneity in parametric production of optical photon pairs. *Physical Review Letters*, 25(2):84, 1970.
- [51] MV Jabir and GK Samanta. Robust, high brightness, degenerate entangled photon source at room temperature. *Scientific reports*, 7(1):1–8, 2017.
- [52] Alexander Lohrmann, Chithrabhanu Perumangatt, Aitor Villar, and Alexander Ling. Broadband pumped polarization entangled photon-pair source in a linear beam displacement interferometer. *Applied Physics Letters*, 116(2):021101, 2020.
- [53] Hugues Guillet de Chatellus, Alexander V Sergienko, Bahaa EA Saleh, Malvin C Teich, and Giovanni Di Giuseppe. Non-collinear and non-degenerate polarization-entangled photon generation via concurrent type-i parametric downconversion in ppln. *Optics express*, 14(21):10060–10072, 2006.
- [54] Aitor Villar, Alexander Lohrmann, and Alexander Ling. Experimental entangled photon pair generation using crystals with parallel optical axes. *Optics express*, 26(10):12396–12402, 2018.
- [55] Paul G Kwiat, Klaus Mattle, Harald Weinfurter, Anton Zeilinger, Alexander V Sergienko, and Yanhua Shih. New high-intensity source of polarization-entangled photon pairs. *Physical Review Letters*, 75(24):4337, 1995.
- [56] Haruka Terashima, Satoshi Kobayashi, Takaho Tsubakiyama, and Kaoru Sanaka. Quantum interferometric generation of polarization entangled photons. *Scientific reports*, 8(1):1–8, 2018.
- [57] A.C. Cardoso, L. P. Berruezo, D. F. Ávila, G. B. Lemos, W. M. Pimenta, C. H. Monken, P. L. Saldanha, and S. Pádua. Classical imaging with undetected light. *Phys. Rev. A*, 97(3):033827, 2018.
- [58] Mikhail I Kolobov, Enno Giese, Samuel Lemieux, Robert Fickler, and Robert W Boyd. Controlling induced coherence for quantum imaging. *Journal of Optics*, 19(5):054003, 2017.
- [59] Anna Paterova, Hongzhi Yang, Chengwu An, Dmitry Kalashnikov, and Leonid Krivitsky. Measurement of infrared optical constants with visible photons. *New Journal of Physics*, 20(4):043015, 2018.
- [60] Chiara Lindner, Sebastian Wolf, Jens Kießling, and Frank Kühnemann. Nonlinear interferometers for broadband mid-infrared spectroscopy. In *Nonlinear Frequency Generation and Conversion: Materials and Devices XIX*, volume 11264, page 112641D. International Society for Optics and Photonics, 2020.
- [61] DB Horoshko, MI Kolobov, F Gumpert, I Shand, F König, and MV Chekhova. Non-linear mach–zehnder interferometer with ultrabroadband squeezed light. *Journal of Modern Optics*, 67(1):41–48, 2020.

- [62] Mirco Kutas, Björn Haase, Patricia Bickert, Felix Riexinger, Daniel Molter, and Georg von Freymann. Terahertz quantum sensing. *Sci. Adv.*, 6(11):eaaz8065, 2020.
- [63] D. A. Kalashnikov, A. V. Paterova, S. P. Kulik, and L. A. Krivitsky. Infrared spectroscopy with visible light. *Nat. Photonics*, 10:98, 2016.
- [64] Anna V. Paterova, Hongzhi Yang, Chengwu An, Dmitry A. Kalashnikov, and Leonid A. Krivitsky. Tunable optical coherence tomography in the infrared range using visible photons. *Quantum Science and Technology*, 3:025008, 2018.
- [65] I. Kviatkovsky, H. M. Chrzanowski, E. G. Avery, H. Bartolomaeus, and S. Ramelow. Microscopy with undetected photons in the mid-infrared. *arXiv:2002.05960*, 2020.
- [66] A. V. Paterova, M. M. Sivakumar, H. Yang, G. Grenci, and L. A. Krivitsky. Hyperspectral infrared microscopy with visible light. *arXiv:2002.05956*, 2020.
- [67] J. Le Gouet, D. Venkatraman, F. N. C. Wong, and J. H. Shapiro. Classical low-coherence interferometry based on broadband parametric fluorescence and amplification. *Opt. Express*, 17:17874, 2009.
- [68] Adam Vallés, Gerard Jiménez, Luis José Salazar-Serrano, and Juan P Torres. Optical sectioning in induced coherence tomography with frequency-entangled photons. *Phys. Rev. A*, 97:023824, 2018.
- [69] Anna V. Paterova, Hongzhi Yang, Chengwu An, Dmitry A. Kalashnikov, and Leonid A. Krivitsky. Tunable optical coherence tomography in the infrared range using visible photons. *Quantum Sci. Technol.*, 3:025008, 2018.
- [70] Aron Vanselow, Paul Kaufmann, Ivan Zorin, Bettina Heise, Helen Chrzanowski, and Sven Ramelow. Mid-infrared frequency-domain optical coherence tomography with undetected photons. In *Quantum Information and Measurement*, pages T5A–86. Optical Society of America, 2019.
- [71] Samuel Lemieux, Mathieu Manceau, Polina R Sharapova, Olga V Tikhonova, Robert W Boyd, Gerd Leuchs, and Maria V Chekhova. Engineering the frequency spectrum of bright squeezed vacuum via group velocity dispersion in an su (1, 1) interferometer. *Physical review letters*, 117(18):183601, 2016.
- [72] Chong-Ki Hong, Zhe-Yu Ou, and Leonard Mandel. Measurement of subpicosecond time intervals between two photons by interference. *Physical review letters*, 59(18):2044, 1987.
- [73] Zu-En Su, Yuan Li, Peter P Rohde, He-Liang Huang, Xi-Lin Wang, Li Li, Nai-Le Liu, Jonathan P Dowling, Chao-Yang Lu, and Jian-Wei Pan. Multiphoton interference in quantum fourier transform circuits and applications to quantum metrology. *Physical review letters*, 119(8):080502, 2017.
- [74] Alexander E Ulanov, Ilya A Fedorov, Demid Sychev, Philippe Grangier, and AI Lvovsky. Loss-tolerant state engineering for quantum-enhanced metrology via the reverse hong–ou–mandel effect. *Nature communications*, 7(1):1–6, 2016.

- [75] C Agnesi, B Da Lio, Daniele Cozzolino, L Cardi, B Ben Bakir, K Hassan, A Della Frera, A Ruggeri, A Giudice, G Vallone, et al. Hong-ou-mandel interference between independent iii-v on silicon waveguide integrated lasers. *Optics letters*, 44(2):271–274, 2019.
- [76] Yuanyuan Chen, Matthias Fink, Fabian Steinlechner, Juan P Torres, and Rupert Ursin. Hong-ou-mandel interferometry on a biphoton beat note. *npj Quantum Information*, 5(1):1–6, 2019.
- [77] Adeline Orioux and Eleni Diamanti. Recent advances on integrated quantum communications. *Journal of Optics*, 18(8):083002, 2016.
- [78] Daniel KL Oi, Alex Ling, Giuseppe Vallone, Paolo Villoresi, Steve Greenland, Emma Kerr, Malcolm Macdonald, Harald Weinfurter, Hans Kuiper, Edoardo Charbon, et al. Cubesat quantum communications mission. *EPJ Quantum Technology*, 4:1–20, 2017.
- [79] Ling Ji, Jun Gao, Ai-Lin Yang, Zhen Feng, Xiao-Feng Lin, Zhong-Gen Li, and Xian-Min Jin. Towards quantum communications in free-space seawater. *Optics Express*, 25(17):19795–19806, 2017.
- [80] Stefanie Barz. Quantum computing with photons: introduction to the circuit model, the one-way quantum computer, and the fundamental principles of photonic experiments. *Journal of Physics B: Atomic, Molecular and Optical Physics*, 48(8):083001, 2015.
- [81] Lucia Caspani, Christian Reimer, Michael Kues, Piotr Roztocky, Matteo Clerici, Benjamin Wetzel, Yoann Jestin, Marcello Ferrera, Marco Peccianti, Alessia Pasquazi, et al. Multifrequency sources of quantum correlated photon pairs on-chip: a path toward integrated quantum frequency combs. *Nanophotonics*, 5(2):351–362, 2016.
- [82] I Ruo Berchera and Ivo Pietro Degiovanni. Quantum imaging with sub-poissonian light: challenges and perspectives in optical metrology. *Metrologia*, 56(2):024001, 2019.
- [83] Alex S Clark, Maria Chekhova, Jonathan CF Matthews, John G Rarity, and Rupert F Oulton. Special topic: Quantum sensing with correlated light sources, 2021.
- [84] Mónica B Agüero. Medición de la evolución temporal del entrelazamiento de una fuente pulsada de pares de fotones entrelazados. In *ANALES AFA*, volume 26, 2015.
- [85] Christian Silva and Juan Vargas. Construcción y caracterización de una fuente de pares de fotones a partir de un cristal ppktp.
- [86] Huan Chen, Silke Auchter, Maximilian Prilmüller, Alexander Schlager, Thomas Kauten, Kaisa Laiho, Benedikt Pressl, Holger Suchomel, Martin Kamp, Sven Höfling, et al. Invited article: Time-bin entangled photon pairs from bragg-reflection waveguides. *APL Photonics*, 3(8):080804, 2018.
- [87] Jie Zhao, Chaoxuan Ma, Michael Rüsing, and Shayan Mookherjea. High quality entangled photon pair generation in periodically poled thin-film lithium niobate waveguides. *Physical review letters*, 124(16):163603, 2020.

- [88] Daniel Huber, Marcus Reindl, Johannes Aberl, Armando Rastelli, and Rinaldo Trotta. Semiconductor quantum dots as an ideal source of polarization-entangled photon pairs on-demand: a review. *Journal of Optics*, 20(7):073002, 2018.
- [89] Dietrich Dehlinger and MW Mitchell. Entangled photon apparatus for the undergraduate laboratory. *American Journal of Physics*, 70(9):898–902, 2002.
- [90] E. J. Galvez, Charles H. Holbrow, M. J. Pysher, J. W. Martin, N. Courtemanche, L. Heilig, and J. Spencer. Interference with correlated photons: Five quantum mechanics experiments for undergraduates. *American Journal of Physics*, 73(2):127–140, 2005.
- [91] Mark Beck. *Quantum Mechanics: Theory and Experiment*. Oxford University Press, 1 edition, 2012.
- [92] Ruediger Scholz and Gunnar Friege. Undergraduate quantum optics : experimental steps to quantum physics Undergraduate quantum optics : experimental steps to quantum physics. *Eur J Phys*, 39:055301, 2018.
- [93] Dorilian Lopez-Mago and Jorge A. Rojas-Santana. Understanding the basic concepts and tools in experimental quantum optics. *Optics Education and Outreach V*, (September):28, 2018.
- [94] PicoQuant. <https://www.picoquant.com/products/category/tcspc-and-time-tagging-modules/picoharp-300-stand-alone-tcspc-module-with-usb-interface>.
- [95] IDQ. <https://https://www.idquantique.com/quantum-sensing/products/id900-time-controller/>.
- [96] Sascha Gaertner, Harald Weinfurter, and Christian Kurtsiefer. Fast and compact multichannel photon coincidence unit for quantum information processing. *Review of Scientific Instruments*, 76(12):123108, 2005.
- [97] Mark F Masters, Tanner Heral, and Kakathi Tummala. Low-cost coincidence counting apparatus for quantum optics investigations. In *ETOP 2015 Proceedings*, page TPE05. Optical Society of America, 2015.
- [98] Byung Kwon Park, Yong-Su Kim, Osung Kwon, Sang-Wook Han, and Sung Moon. High-performance reconfigurable coincidence counting unit based on a field programmable gate array. *Appl. Opt.*, 54(15):4727–4731, may 2015.
- [99] Jorge Arturo Rojas-Santana. Simulation of time-correlated and time-uncorrelated photons. <https://www.mathworks.com/matlabcentral/fileexchange/69960-simulation-of-time-correlated-and-time-uncorrelated-photons>, MATLAB Central File Exchange. (Retrieved March 28, 2019).

- [100] Jorge Arturo Rojas-Santana. Oscilloscope automatization for photon counting and timing. <https://www.mathworks.com/matlabcentral/fileexchange/69962-oscilloscope-automatization-for-photon-counting-and-timing>, MATLAB Central File Exchange. (Retrieved March 28, 2019).
- [101] Jorge Arturo Rojas-Santana. Coincidence histogram of correlated photons. <https://www.mathworks.com/matlabcentral/fileexchange/69979-coincidence-histogram-of-correlated-photons>, MATLAB Central File Exchange. (Retrieved March 28, 2019).
- [102] Marta Gilaberte Basset, Josué R León Torres, Tobias B Gäbler, and Markus Gräfe. Ultra-stable quantum imaging with undetected photons in video rate. In *Quantum 2.0*, pages QTh7B–8. Optical Society of America, 2020.
- [103] Pablo Yepiz Graciano, Alí Michel Angulo Martínez, Dorilian Lopez-Mago, Gustavo Castro-Olvera, Martha Rosete-Aguilar, Jesús Garduño-Mejía, Roberto Ramírez Alarcón, Héctor Cruz Ramírez, and Alfred B. U’Ren. Interference effects in quantum-optical coherence tomography using spectrally engineered photon pairs. *Scientific Reports*, 9:8954, 2019.
- [104] Pablo Yepiz-Graciano, Alí Michel Angulo Martínez, Dorilian Lopez-Mago, Hector Cruz-Ramirez, and Alfred B U’Ren. Spectrally resolved hong–ou–mandel interferometry for quantum-optical coherence tomography. *Photonics Research*, 8:1023–1034, 2020.
- [105] Zeferino Ibarra-Borja, Carlos Sevilla-Gutiérrez, Roberto Ramírez-Alarcón, Hector Cruz-Ramírez, and Alfred B. U’Ren. Experimental demonstration of full-field quantum optical coherence tomography. *Photonics Res.*, 8(1):51, jan 2020.
- [106] Maged B Nasr, Darryl P Goode, Nam Nguyen, Guoxin Rong, Linglu Yang, Björn M Reinhard, Bahaa EA Saleh, and Malvin C Teich. Quantum optical coherence tomography of a biological sample. *Optics Communications*, 282(6):1154–1159, 2009.
- [107] Malvin Carl Teich, Bahaa EA Saleh, Franco NC Wong, and Jeffrey H Shapiro. Variations on the theme of quantum optical coherence tomography: a review. *Quantum Information Processing*, 11(4):903–923, 2012.
- [108] Dorilian Lopez-Mago and Lukas Novotny. Quantum-optical coherence tomography with collinear entangled photons. *Opt. Lett.*, 37(19):4077, oct 2012.
- [109] X. Y. Zou, T. P. Grayson, and L. Mandel. Observation of quantum interference effects in the frequency domain. *Phys. Rev. Lett.*, 69:3041, 1992.
- [110] Armin Hochrainer, Mayukh Lahiri, Radek Lapkiewicz, Gabriela B Lemos, and Anton Zeilinger. Interference fringes controlled by noninterfering photons. *Optica*, 4(3):341–344, 2017.

- [111] Axel Heuer, Sebastian Raabe, and Ralf Menzel. Phase memory across two single-photon interferometers including wavelength conversion. *Physical Review A*, 90(4):045803, 2014.
- [112] C. You, S. Adhikari, X. Ma, M. Sasaki, M. Takeoka, and J. P. Dowling. Conclusive precision bounds for SU(1,1) interferometers. *Phys. Rev. A*, 99:042122, 2019.
- [113] N. R. Miller, S. Ramelow, and W. N. Plick. Super-sensitive metrology using induced coherence. *arXiv:1907.09004*, 2020.
- [114] W. Wasilewski, A. I. Lvovsky, K. Banaszek, and C. Radzewicz. Pulsed squeezed light: Simultaneous squeezing of multiple modes. *Phys. Rev. A*, 73:063819, 2006.
- [115] J. P. Torres, K. Banaszek, and I. A. Walmsley. Engineering nonlinear optic sources of photonic entanglement. *Progress in Optics*, 56:227, 2011.
- [116] B. Dayan. Theory of two-photon interactions with broadband down-converted light and entangled photons. *Phys. Rev. A*, 76:043813, 2007.
- [117] H. A. Haus. Electromagnetic noise and quantum optical measurements. *Springer Verlag*, 2000.
- [118] Robert W. Boyd, Girish S. Agarwal, Clifford Chan, Kam Wai, Anand Kumar Jha, and Malcolm N. O’Sullivan. Propagation of quantum states of light through absorbing and amplifying media. *Opt. Comm.*, 281:3732, 2008.
- [119] Covesion Ltd. <https://www.covesion.com>.
- [120] Menlo Systems. <https://www.menlosystems.com>.
- [121] Leica Microsystems. <https://www.leica-microsystems.com>.
- [122] Yoon-Ho Kim, M.V. Chekhova, S.P. Kulik, Yanhua Shih, and M.H. Rubin. First-order interference of nonclassical light emitted spontaneously at different times. *Phys. Rev. A*, 61:051803, 2000.
- [123] Iagoba Apellaniz, Matthias Kleinmann, Otfried Gühne, and Géza Tóth. Optimal witnessing of the quantum fisher information with few measurements. *Physical Review A*, 95(3):032330, 2017.
- [124] Yiyu Zhou, Jing Yang, Jeremy D Hassett, Seyed Mohammad Hashemi Rafsanjani, Mohammad Mirhosseini, A Nick Vamivakas, Andrew N Jordan, Zhimin Shi, and Robert W Boyd. Quantum-limited estimation of the axial separation of two incoherent point sources. *Optica*, 6(5):534–541, 2019.
- [125] J Řeháček, M Paúr, B Stoklasa, D Koutný, Z Hradil, and LL Sánchez-Soto. Intensity-based axial localization at the quantum limit. *Physical review letters*, 123(19):193601, 2019.

- [126] T. B. Dubose, D. Cunefare, E. Cole, P. Milanfar, J. A. Izatt, and S. Farsiu. Statistical models of signal and noise and fundamental limits of segmentation accuracy in retinal optical coherence tomography. *IEEE Transactions on Medical Imaging*, 37(9):1978–1988, 2018.
- [127] Di Xu, Andres Garcia Coletto, Zhenkun Wen, Benjamin Moon, Jonathan C Papa, Michael Pomerantz, John C Lambropoulos, and Jannick P Rolland. Cascade optical coherence tomography (c-oct) towards freeform metrology. In *Interferometry XX*, volume 11490, page 114900K. International Society for Optics and Photonics, 2020.

Curriculum Vitae

Doctorate student Jorge Arturo Rojas Santana was born in Toluca, México, on August 22, 1987. He earned the MSc. in Optics degree from the Center for Scientific Research and Higher Education at Ensenada in February 2014 and BS. in Physics degree from the Autonomous University of the State of Mexico in June 2010. He was accepted in the graduate programs in Nanotechnology in January 2018.

This document was typed in using L^AT_EX 2_ε^a by Jorge Arturo Rojas Santana.

^aThe style file `phdThesisFormat.sty` used to set up this thesis was prepared by the Center of Intelligent Systems of the Instituto Tecnológico y de Estudios Superiores de Monterrey, Monterrey Campus